THESIS

PRELIMINARY DEVELOPMENT AND TESTING OF AN OPEN-PATH HYDROCARBON SENSOR FOR OIL AND GAS FACILITY MONITORING

Submitted by

Betsy M. Farris

Department of Mechanical Engineering

In partial fulfilment of the requirements

For the Degree of Master of Science

Colorado State University

Fort Collins, Colorado

Summer 2019

Master's Committee:

Advisor: Azer P. Yalin

Emily V. Fischer
Shantanu H. Jathar

ABSTRACT

PRELIMINARY DEVELOPMENT AND TESTING OF AN OPEN-PATH HYDROCARBON SENSOR FOR OIL AND GAS FACILITY MONITORING

We developed an open-path laser absorption sensor for detection of unspeciated hydrocarbons for oil and gas production facility fence line monitoring. Such sensors can aid in maintaining air quality standards by quantifying greenhouse gas emissions and detecting emissions that cause adverse health effects. Our initial design employs a single-path detection system, though future implementations may use multiple paths for large-scale facility monitoring. The sensor uses a compact mid-infrared laser source in the spectral region of ~3.3 μm to measure absorption of several hydrocarbon species and is intended for open-paths of ~100 m to 1 km. Spectral simulations show that for typical conditions the hydrocarbons cause a transmission reduction of ~10% allowing for a robust measurement.

The initial prototype system uses a helium-neon (He:Ne) laser at 3.391 μm for which signal contributions from methane and non-methane hydrocarbons are comparable. Closed-cell tests were performed with diluted methane (~150-250 ppm) to validate the transmission signals and showed good agreement with expected (calculated) values to within ~10%. The system employs a reference leg, with a 2nd detector (near the source), to normalize for laser power fluctuations. For improved signal-to-noise, particularly for detection of small concentrations and transmission changes, we employ phase-sensitive detection with a mechanical chopper and software based lock-in amplifier. This detection scheme, when employed in the field, allows measurement of transmission signals with stability <0.5% (based on coefficient of variation over 60 s).

The portable field sensor system uses two refractive telescopes (2" diameter optics), a transmitter and receiver co-located on a mobile optical breadboard, and a reflector dictating the pathlength. We performed initial tests with pathlengths up to ~25 m (one way), though the design should allow paths in excess of 100 m. Methane was released for initial field tests at known flow rates near the center of the beam path. Transmission signals in agreement with expectations (given uncertainties in the wind and plume dispersion) were observed. The system should allow detection of leaks (emissions) for mass flows as low as ~0.1 g/s of methane (or equivalent optical signal from other species resulting in a 1% change in signal) for the case where the source is ~150 m from the beam path and under typical atmospheric conditions. Recommendations for future modifications are provided based on potential shortcomings identified by initial field testing. Initial field testing also proved that this technology could be a viable low-cost solution for hydrocarbon detection.

ACKNOWLEDGMENTS

I would like to acknowledge and thank Azer Yalin for all of his guidance and support. I am especially grateful for his willingness to allow me to pursue my interests and passions in air quality within and beyond the scope of this project. Allowing me to lead Space Grant and to take a summer internship greatly enriched my experience and better positioned me to find fulfilling work outside of school. Finally, I will be forever grateful for his assemblage of such an excellent research group. I knew joining this group would mean long hours, but would also result in excellent learning opportunities and huge personal growth. The Center for Laser Sensing and Diagnostics has provided me with the training, support, and hands-on learning experiences necessary to accomplish this work and to grow as an engineer. I am so grateful for everything I learned from Laurie McHale, Soran Shadman, Adam Friss, Ciprian Dumitrache, Charles Rose, and many other students. I am especially thankful for their willingness to help me lug my experiment all around town and the lab. I feel very grateful for all the Powerhouse students, faculty, and staff who helped me perform this work and kept me sane. I would also like to thank Eben Thoma of the Environmental Protection Agency and Parikshit Deshmukh of Jacobs Technology for supporting this work as well as providing technical guidance. Finally, a huge thanks goes to my friends and family. I am very lucky to have such an amazing support system. I could not have done this without you!

TABLE OF CONTENTS

LIST OF TABLES

LIST OF FIGURES

CHAPTER 1:

Introduction

1.1 Hydrocarbons, Methane, and Volatile Organic Compounds

Monitoring hydrocarbon emissions from oil and gas facilities is important for human health, global warming, and mitigating waste for producers and consumers. Hydrocarbons are defined as organic species containing carbon and hydrogen atoms. Some hydrocarbons are classified as volatile organic compounds (VOCs). These species are typically defined as having high vapor pressure in ambient conditions. These categories can overlap and each have different implications for climate, human health, and the environment. While the technology developed in this thesis is applicable for many pollutants emitted from industrial activities, this thesis studies the feasibility of detecting hydrocarbon species from oil and gas activities which include methane (CH_4) and non-methane VOCs (NMVOCs).

The majority of the energy consumed in the United States is from natural gas and petroleum fuel. In 2017, 37% of consumed energy came from petroleum, 29% was from natural gas, and 14% from coal[1]. All fossil fuels produce greenhouse gases — mainly carbon dioxide (CO_2) — when combusted. The increase in consumption of natural gas and renewables as opposed to coal has contributed to a decrease in CO_2 production. This is partially due to natural gas producing fewer CO_2 molecules than coal and petroleum during combustion[2]. Natural gas is often presented as a "bridge fuel" to renewables because of its ability to lower greenhouse gas emissions, produce fewer hazardous particulates, and decrease sulfur dioxide (SO_2) emissions in comparison to coal when used over a strategic timespace[3]. However, the benefits of transitioning from coal to natural gas decrease rapidly if the natural gas is emitted without being burned.

CH_4 is the primary species (60-90% by molecule) in most natural gas mixtures[4]. The global warming potential of CH_4 makes this fuel a dangerous liability to the global budget of greenhouse gases. The Intergovernmental Panel on Climate Change describes CH_4's 20 year Global Warming Potential as 84x that of CO_2[5]. Thus, fugitive emissions of CH_4 can negate the positive impacts of switching from conventional fuels — such as coal — to natural gas. This has resulted in higher scrutiny of the natural gas industry to quantity the amount of CH_4 being released during production, transportation, and use.

Many NMVOCs are hazardous air pollutants that can cause can harm to humans when inhaled[6]. NMVOCs are also ozone precursors; ozone is harmful when inhaled and detrimental to vegetation[7]. The oil and gas industry is one of the largest industrial sources of NMVOCs. Typical NMVOCs emitted from oil and gas facilities include alkanes, cycloalkanes, aromatics, alkenes, and alkynes[8]. A study estimated that alkanes from oil and natural gas contributed to approximately 20% of the summertime photochemical ozone production in the Colorado Front Range[9]. The National Ambient Air Quality Standard for ground-level ozone was recently lowered from 75 to 70 parts per billion (ppb)[10]. In the Oct. 20, 2016, the United States Environmental Protection Agency (EPA) issued control techniques guidelines for reducing VOC emissions from oil and gas activity which included monitoring of fugitive emissions[11]. This was recommended as a part of the EPA's strategy for reduction CH_4 and ozone-forming pollution from the oil and natural gas industry[12]. The initial motivation for this thesis was to research the feasibility of creating a low-cost sensor for facility monitoring of NMVOCs. The application and development of this technology was expanded to include CH_4 detection while exploring trades for the sensor's architecture.

1.2 Facility Monitoring

The ultimate application of this sensor is to detect hydrocarbon emissions from oil and gas facilities. For the context of this thesis, "facility" is defined generally to include small scale operations (e.g. a single well pad) and large scale operations (e.g. a refinery). This section explains the importance of facility monitoring. There are new concerns for the public due to advancements in extraction technology for natural gas. Unconventional methods, such as hydraulic fracturing and horizontal drilling, have made it easier to access reserves previously out of reach. Increases in extraction bring operations closer to populated areas. This growth, paired with population growth and the affordability of housing nearby oil and gas wells, is also a concern for environmental justice[13]. Another study from the Colorado Front Range found that air pollutant concentrations and health risks, characterized by non-CH_4 hydrocarbon inhalation exposure, increased with proximity to oil and gas facilities[6].

Unintended emission of hydrocarbons from oil and gas facilities can also be a loss of product for oil and gas companies as well as a safety concern for operators or technicians. Monitoring an area along the full fence line of a facility can ensure that the fugitive emissions are detected regardless of the wind direction or configuration of the site. Such approaches can be implemented for flux measurements, alarm systems, or both. The technology developed in this thesis is applicable over length scales of ~10-1000 m. The South Coast Air Quality Management District, as of January 2019, was reviewing Rule 1180 which will "require real-time fence line air monitoring systems and to establish a fee schedule to fund refinery-related community air monitoring systems that provide air quality information to the public about levels of various criteria air pollutants, volatile organic compounds, metals, and other compounds, at or near the property boundaries of petroleum refineries and in nearby communities[14]." This regulation

proposes monitoring criteria air pollutants, specific NMVOCs such as formaldehyde, BTEX compounds (benzene, toluene, ethylbenzene, and xylenes) and non-CH_4 hydrocarbons.

Finally, a significant motivation for pursuing the development of a low-cost fence line detection system at facilities is for detection of large emission events. Some large emissions are planned, such as condensate flashing and liquid unloading; however, Zavala-Araiza et al. (2017) determined that abnormal process conditions, such as malfunctioning equipment, can also contribute to a significant proportion of a site's emissions[15]. Super-emitters, as defined by their study, are unintended emissions larger than 26 kg CH_4 per hour (Figure 1). This threshold was chosen "as it corresponds to the highest-emitting 1% of sites in the site-based distribution, accounting for 44% of total site emissions" for the given study in the Barnett Shale[15].

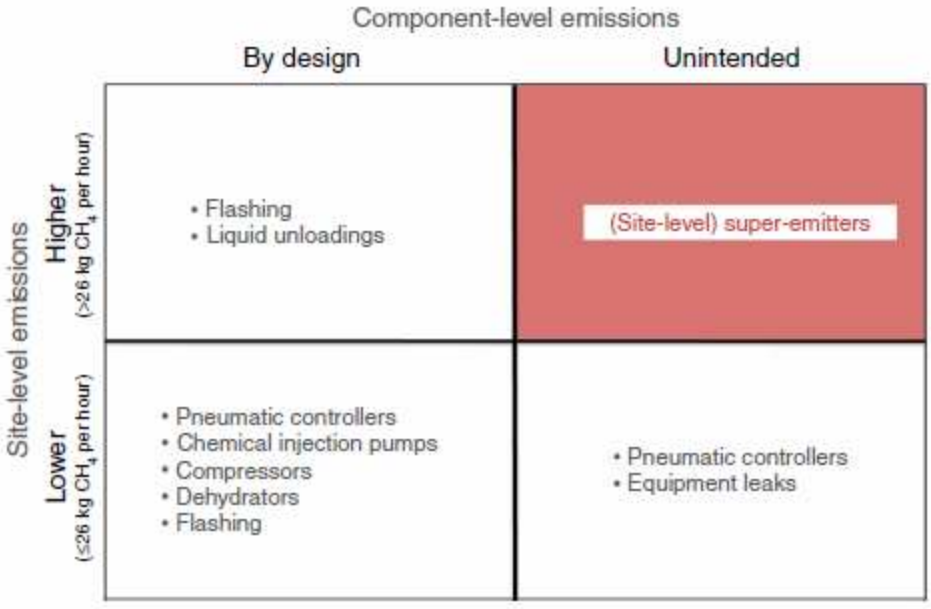

Figure 1: Classification of sites in terms of magnitude of emissions and component behavior[15].

In another effort to quantify CH_4 emissions from natural gas systems, one group evaluated ~15,000 measurements from 18 studies to conclude that the largest 5% of emissions account for 50% of the total leaked volume[16]. It was concluded that many of these events result in an

underestimation of emissions using standard methods and inventories, the so called "fat tail" distinction[17]. One study concluded that "approximately 1 in 25 facilities exhibits super-emitter emissions during any given hour of the year"[18]. This low-cost sensor concept looks at the feasibility of detecting average emissions, but it would be best used for the detection of super-emitters or large releases of both CH_4 and NMVOCs.

1.3 Current Monitoring Techniques

This section provides an overview of current techniques for monitoring NMVOCs, CH_4, and other pollutants from oil and gas activities, as well as related technologies that could be used in a similar application. The purpose of this section is to discuss the applicability of each technology for facility monitoring and its potential to be used as a low-cost (less than ~$10,000 to $50,000) detection method. The cost, complexity, and detection limits of each technique, e.g. laboratory-grade gas chromatography, citizen science, open path, and in situ sensors, vary greatly.

The Environmental Protection Agency compiled a Compendium of Methods for the Determination of Toxic Organic Compounds in Ambient Air which lists the preferred detection method for different ambient air pollutants[19]. All methods for NMVOC detection require collecting the sample for the exception of FTIR Open Path Spectroscopy. EPA Method 325A details sampler deployment and NMVOC sample collection for NMVOCs from fugitive and area sources[20].

The first detection method presented is the use of canisters and the Tracer Ratio Method which includes a description of gas chromatography. The Tracer Ratio Method is a detection technique wherein a passive gas is released at a known emission rate at the location of the emission source being measured. The emission rate of the passive gas, or tracer gas, is multiplied by the ratio of the measured species concentration and the concentration of the tracer gas[21]. This

technique was used in a study by Collett et al. for measuring NMVOCs from natural gas drilling and well completion in Garfield County, Colorado[22]. These emission rates of NMVOCs and CH_4 were used to establish order of magnitude requirements for our proposed sensor. This study used acetylene for the tracer gas as it is not emitted from oil and gas operations and is present at low background mixing ratios. CH_4 was detected downwind with a Picarro G2203, a cavity ring-down spectroscopy sensor, and NMVOCs were analyzed with an advanced canister system. Total air measurements from the canisters were processed in a GC-FID (gas chromatography with flame-ionization detection) system allowing for speciation of up to 48 different species.

This measurement technique, gas chromatography (GC) with flame ionization detection (FID), is often used in measuring NMVOCs[23]. Gas chromatography is a technique used in analytical chemistry for separating species by how long it takes each species to react with a stationary phase (known as a species' "retention time"). After species are separated with GC, flame ionization detectors (FIDs) or other detection methods quantify and identify the species in each sample[24]. Mass spectrometry (MS) is another common detection method for the speciation of the collected NMVOCs with GC. Both MS and FID rely on the ionization of the sample to identify and measure the abundance of a given species. FIDs count the carbon molecules ionized in a flame, while MS uses an ion-generating source and then calculates a mass to ion ratio. The analysis takes time and is often done offsite. If identifying specific species and their concentrations to fine resolutions is the goal, this method is the most appropriate.

The next detection method is summarized by an overview of in situ sensors used for hydrocarbon detection. In situ sensors come in a wide variety ranging from expensive research grade to consumer off the shelf (COTS) sensors. Spinelle et al. presents a list from a literature review on low cost sensor technologies for benzene monitoring and other NMVOCs:

- "Photo-ionization detectors (PID), both portable hand held instrument and Original Equipment Manufacturers (OEMs),
- OEM electrochemical sensors either of amperometric or potentiometric type,
- OEM metal oxide sensors (MOx) with change of conductivity instead of chemical reaction,
- Optical sensors including UV portable spectrometers,
- Portable or micro-gas chromatograph (μGC) that combines micro column with MOx or PID OEM as detectors. Flame ionization detectors (FID) are generally not considered in this review because of the need of an external hydrogen source for operation. Bench top instruments are excluded in this category for the lack of handiness and their high price range,
- and electronic noses and sensor-arrays" [25]

Many of these types of sensors can be used as a fence line monitoring system or network if placed around a source. The COTS sensors can be extremely low cost, even in larger quantities, and can be sold with consumer-ready packaging. For example, g. the Adafruit CCS811 Air Quality Sensor Breakout - VOC and eCO2 measures TVOC (Total Volatile Organic Compound) concentrations within a range of 0 to 1187 parts per billion (ppb) using a CCS811 chip that detects VOCs using a metal oxide sensor and includes an Analog-to-Digital converter and an I_2C interface and costs $19.95. While such systems may seem plug-and-play, the reliability and accuracy of these sensors depend highly on their placement, temperature and humidity, and require calibration against a trusted source. Collier-Oxandale et al. performed a rigorous analysis to determine ideal deployment methods for the use of low-cost sensors for CO_2 and O_3 measurements in building and neighborhood environments[26]. Their conclusions provide details on how to calibrate and where to place sensors as well as suggestions for documentation and data analysis. Their conclusion that sensors should be placed both up and downwind from the source is highly applicable for facility monitoring applications.

Different techniques for monitoring an open path for hydrocarbons are discussed in detail. Open-path (OP) technologies allow for fewer sensors along the fence line and can operate in convenient, monostatic configurations where the source (typically a laser) and detector are on the

same platform. The standard for these types of sensors includes open-path Fourier transform infrared spectrometers (OP-FTIR) and infrared video analysis. According to an EPA summary, OP-FTIR saves money and time with multi-gas analysis where the "path-integrated pollutant concentration measurement minimizes possible sample contamination and provides real-time pollutant concentration"[19]. OP configurations can also allow for measurements in locations which are too difficult to retrieve a canister or passive sample. They operate by modulating infrared (IR) radiation with an interferometer and often employ corner-cube retroreflectors to return light to the receiver[27]. The concentration measurement will consist of a mixing ratio and pathlength (path integrated, e.g. ppm-m). The disadvantages of OP-FTIR systems include requiring a trained operator, size, and cost. Systems can range between tens of thousands to more than one hundred thousand dollars for a given application which provides the basis for defining "low cost" as anything less than $10,000 to $50,000.

The EPA, in 2009, fielded OP-FTIR systems to measure the NMVOC emissions from oil and gas produced water evaporation ponds[28]. Like other campaigns, an alkane mixture was most prevalent in their measurements, and many other NMVOCs were below detection limits of their system. They deployed the OP-FTIR in a four corner configuration to obtain a path-integrated concentration and also employed a "vertical radial plume mapping (VRPM) plane-integrated computer algorithm with the acquired multi-path PIC data and wind vector information as the primary inputs"[28]. The detection limits of the OP-FTIR for most VOC species were in the 10s of ppb.

Another solution for CH_4 and NMVOC detection along an open path is the use of video imagery which can be performed with commercial cameras for less than $10,000. The cost of this monitoring technique can, however, be much more expensive depending on the spectral bands

used or the sophistication of the system. Sandsten et al. uses a thermal camera to detect ammonia, ethylene and CH_4 from gas leaks[29]. CH_4 detection was done in the 7-8.5 µm range. A gas-correlation method is used to detect species that have over-lapping spectral regions. Similarly, another method is to employ an adaptive background subtraction in the wavelet domain of visible range video footage to detect VOCs due to their change in temperature when being leaked from an oil and gas source[30]. Certain thresholds were developed to allow for the detection of leaks without falsely identifying image changes from moving leaves or shadows.

The final few detection methods detailed in this section employ lasers or light sources, but are less standard than the OP-FTIR systems. The use of lasers in monitoring technology may put the instrument cost above well above the cost of many COTS in situ sensors. However, in some cases, lasers can allow for detection methods that are cheaper and less labor intensive than canister measurements or OP-FTIR. Differential absorption light detection and ranging (DIAL) was used to measure $>C_2$ hydrocarbons, CH_4, and benzene with a system that employed two pulsed lasers at different wavelengths to detect species in the light's path (Figure 2)[31]. The DIAL instrument, while considered mobile, required a 12 m trailer to store and operate the equipment, but consequently was capable of measuring over a 500 m pathlength and scanning vertically 50 m.

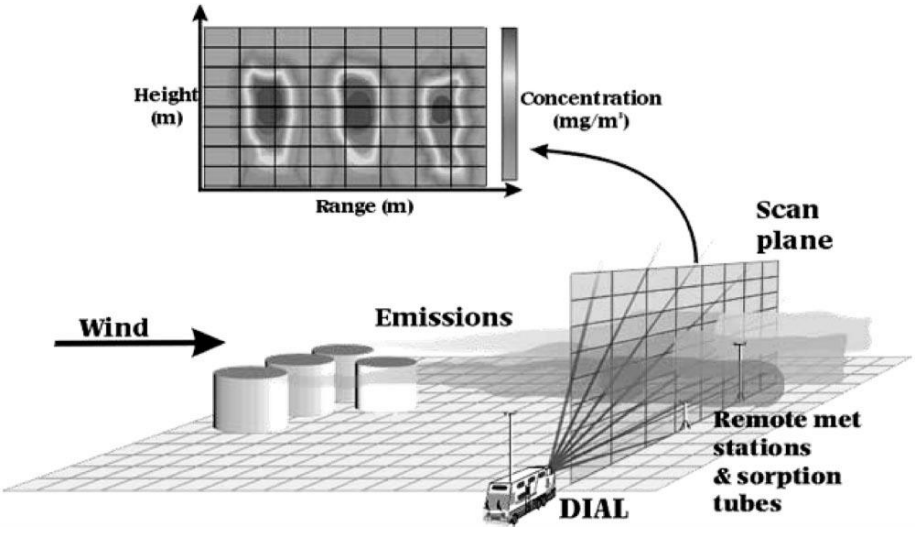

Figure 2: Schematic of DIAL system measuring emissions[31].

Vita et al. also present a differential measurement over a long path (400 m) to measure sulfur dioxide (SO_2) and other volatile species from volcanic gas at a lower-cost measurement technique than OP-FTIR[32]. Their application of long-path differential optical absorption spectroscopy (LP-DOAS) allows for a portable instrument with fewer optical components than DIAL or OP-FTIR. Their technology uses a monostatic design and a retroreflector as well as UV LEDs as the light source (Figure 3).

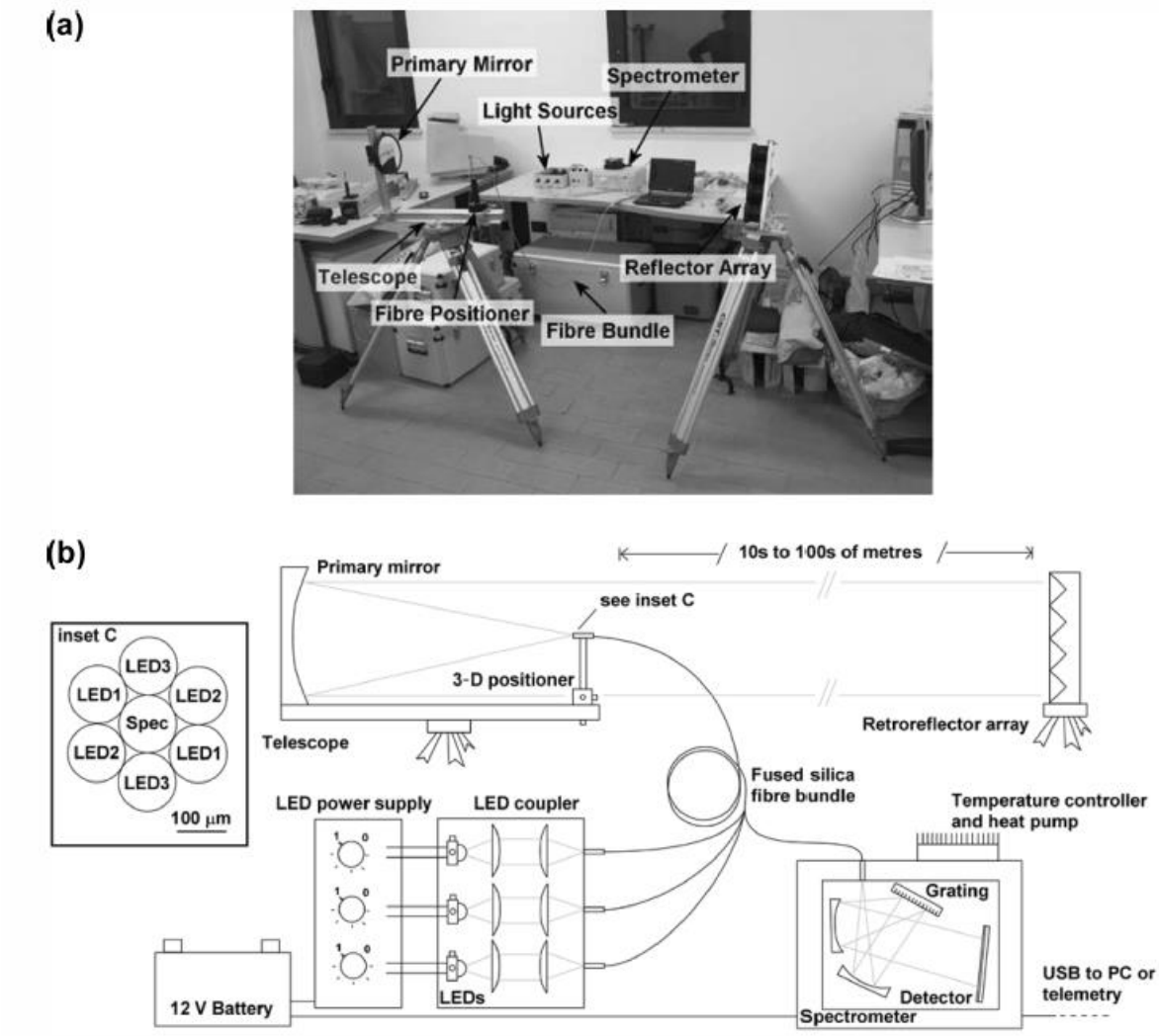

Figure 3: Photograph (a) and schematic (b) of the portable active long-path DOAS instrument. Light from three UV LEDs is coupled to a fibre bundle, collimated to a parallel beam and sent to an array of reflectors. Upon returning, it is coupled to a moderate-resolution UV spectrometer for analysis of absorption features[32].

Vita et al. suggests near-infrared tunable diode laser absorption spectroscopy (NIR-TDLAS) as an alternative to DOAS that would provide an even simpler instrument and notes the applicability for CH_4. TDLAS has been used for CH_4 detection in a simplified open-path configuration by Xia et al[33]. In this instrument, two distributed feedback (DFB) diode lasers at 1.65 and 1.58 μm are used. One laser is scanned over an absorption feature and the other emits at

a fixed wavelength off of the absorption feature. Both signals are modulated such that the return signals are then processed in a lock-in amplifier (Figure 4).

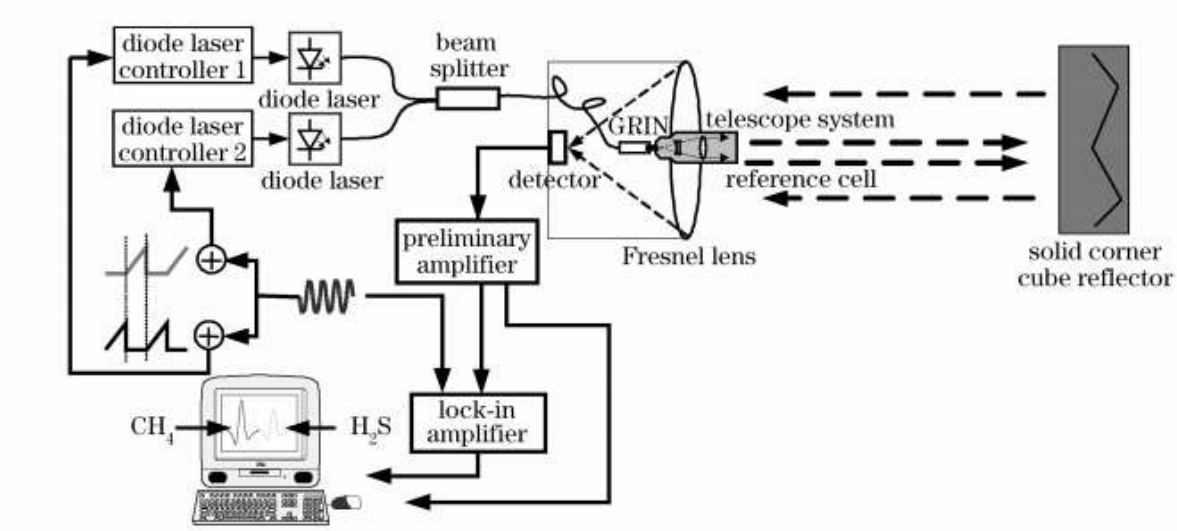

Figure 4: Schematic of the time-sharing scanning open-path TDLAS system[33].

Finally, laser diode technology in the mid-infrared has progressed rapidly. Quantum cascade lasers (QCLs) and interband cascade lasers (ICLs) have enabled measurements in the mid-infrared[34]. These lasers, similar to those used in TDLAS, provide advantages for deployed or mobile systems as they are often small, low power, eye-safe, and tunable over a wide range. The Quantum Cascade Laser Open-Path System (QCLOPS) was designed to monitor ozone, ammonia, and CO_2 in the lower atmosphere[35]. The use of QCL allows for tunablity over absorption features of multiple species over pathlengths 0.1 to 1.0 km. Like the TDLAS system, this sensor is monostatic with the detector and associated telescope collocated with the laser. The test setup deploys the instrument inside a building and has a single retroreflector 38 m away creating a 76 m pathlength.

There are other advanced laser-based systems such as cavity ring down spectroscopy[36] or pulse width modulation systems[37] that are capable of detecting certain VOCs and CH_4 at very low

concentrations over short pathlengths. However, low-cost facility monitoring does not require such capabilities but, instead, requires open-path configurations over many meters.

High-performance instruments and measurement systems for hydrocarbon detection can provide highly sensitive measurements with chemical speciation in near real time. This can be done with many point measurements or a few open-path systems. However, currently, there is insufficient voluntary use of high-performance fence line monitoring systems for facilities in industry[38]. Therefore, there is a need for low-cost systems that can provide a simple detection technique for significant emission events. Such systems will not be able provide precision measurements but can be used as an alarm system or method for process control to allow facilities to minimize their unwanted and unplanned fugitive emissions.

1.4 Objectives and Outline

The objective of this thesis is to demonstrate a proof-of-concept, low-cost sensor for detecting hydrocarbon emissions from oil and gas facilities. The development and testing of this sensor revealed the limitations of producing this technology with off-the-shelf components. The results from this work identified potential improvements to this technology for future iterations. This thesis was motivated by these objectives:

- Design an open-path laser absorption sensor for unspeciated hydrocarbons capable of being deployed for fence line detection at a significantly lower cost than OP-FTIR systems.
- Build, and test in the lab, a proof-of-concept breadboard version of the sensor.
- Preform preliminary field testing to evaluate and prioritize future work that would allow the detection method to remain low-cost while advancing field capabilities.

Chapter 2 uses results from previous field studies and a Gaussian plume model to perform an initial analysis to determine if the proposed detection technique, direct absorption spectroscopy, is applicable for the potential emissions common to facilities. Chapter 3 discusses sensor hardware development and lab testing. Chapter 4 presents the initial field testing results. Chapter 5 discusses conclusions and future work.

CHAPTER 2:

Spectral Simulation of Sensor and Plume Model

This chapter outlines the assumptions and methods used for sensor design. The detection technique, direct absorption spectroscopy, was chosen due to the selected species relevant to this application and their absorption spectra. Spectral simulations were guided by information from spectral datasets and concentrations from past field campaigns as well as constraints from test equipment. A plume model was developed to apply the spectral simulations to a physical model for predicting sensor response.

2.1 Direct Absorption Spectroscopy

Spectroscopy is the measurement of spectra produced by the interaction of electromagnetic radiation with matter. The fundamental technique used in this sensor development is direct absorption spectroscopy (DAS). This technique allows for the detection of species by measuring the energy absorbed by a molecule through rotational, vibrational or electronic transitions. Measurement of the concentration of any given chemical compound is possible because of the Beer-Lambert Law that states the "intensity of a beam of monochromatic light decreases exponentially with the increase in concentration of the absorbing substance arithmetically"[39]. For the operation of this sensor, the monochromatic light is supplied by a laser source. Equation 2.1 is the fundamental equation used to determine the concentration of a species using direct absorption.

$$I = I_0 \exp\big(-A(\lambda)\big) = I_0 exp(-k(\lambda)L) \tag{2.1}$$

where I_0 is the initial light intensity from the laser, $A(\lambda)$ is the dimensionless absorbance for a molecular species at a specific wavelength of light which is found from the absorption coefficient,

$k(\lambda)$ in cm^{-1}, and the length, L in cm. The value of $k(\lambda)$ is determined (scaled by) the concentration of a species. Figure 5 depicts a simplification of the absorption of light from a laser source and the resultant decrease in intensity as the light reaches the detector. The distance between the laser and detector is the pathlength or L from Equation 2.1. Absorption, in this method, is a path-integrated, line of sight measurement.

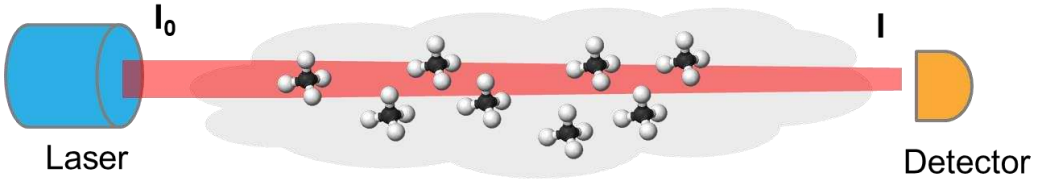

Figure 5: Direct absorption measurement technique with initial (I_0) and measured intensity (I).

DAS is defined by the change in light intensity received by the sensor, used to calculate the absorbance for the given medium. Beer-Lambert's law can be inverted to calculate absorbance (A) and concentration.

$$A(\lambda) = -\ln\left(\frac{I}{I_0}\right) = -\ln(T) \tag{2.2}$$

$$k(\lambda) = A/L \tag{2.3}$$

Absorbance can be computed from experimental data by taking the ratio of the measured intensity (I) and initial intensity (I_0). The ratio of the signals (Equation 2.2) can also be defined as the transmittance, T. Therefore, the absorption coefficient, $k(\lambda)$, is the experimental absorbance per length which can be compared to spectral databases to calculate concentration (Equation 2.3).

The change in intensity across an open path through the atmosphere will be from absorption but also from scattering. The loss of light due to both absorption and scattering is extinction. While a direct comparison of initial and final intensity will be a true extinction measurement, we are assuming that any change in scattering due to ambient aerosols or other molecules will constant

for the sample, i.e. the same for the initial and final intensity measurement. Extinction from ambient aerosols may be a concern over large (many kilometer) pathlengths, but will not be significant for this initial sensor design[40]. For this design, we will assume that the change in light intensity is due only to absorption. This detection method will able to measure a relative concentration above background along its pathlength due to absorption.

Using this principal, the design of a direct absorption system requires knowing expected concentrations, availability of light sources, the spectra or absorption characteristics of the species at given wavelengths, and pathlengths needed for detection. If the absorption at any wavelength associated with a species of interest is low relative to the limit of quantification, a longer pathlength is needed in order to increase the drop in intensity past that limit. Often sensor technologies create longer pathlengths across a sample to allow for the detection of very low concentrations of species. A multi-pass cell can be used with two reflective surfaces such that a beam passes through a sample multiple times creating an effective pathlength that is larger than the sensor's physical length. Such configurations require large optics and are very challenging to align, especially if attempting to create a cell with hundreds of passes[41]. Cavity enhanced absorption spectroscopy (CEAS) and cavity ring-down spectroscopy (CRDS) use high-finesse cavities and base the measurement on the time it takes for the light to decay from the cavity[42]. These methods can increase the pathlength by 10^5 or greater when compared to conventional absorption spectroscopy[43]. Many optical sensors also take advantage of phase-sensitive detection (PSD) by using lock-in amplifiers (LIAs) which multiply and filter a reference signal and a modulated input to attenuate unwanted noise, a method capable of detecting signals even a thousand times smaller than the sources of noise[44,45].

In many cases, the more complicated the spectroscopic technique, the lower the detection limit, but this comes at a higher price point. Therefore, direct absorption offers a simplified

detection method with the capability of a system being created with only COTS optics. As discussed in Chapter 1, the detection and mitigation of super-emitters and large sources can significantly minimize the harm caused by facility emissions. This technology seeks to exploit DAS's low-cost potential while also designing for the capability to detect species at concentrations common in unwanted emissions from oil and gas facilities.

2.2 Absorption Spectra

To be able to choose equipment for DAS, it is necessary to understand the absorption spectra of the species being detected as well as their concentrations. This section details how spectra were chosen, the findings from applying the spectral simulation to a Gaussian plume model, and how these results validate the detection of CH_4 and NMVOCs. Multiple species were analyzed at concentrations from the Collett et al. study[22], referred to as the Garfield Study, and a study from Thoma et al.[28], which will be referred to as the EPA Ponds Study. The main rational of choosing species from relevant studies was to obtain an order of magnitude estimation of the detection limits feasible with the proposed laser and pathlengths, and, thereby, determining the applicability of the proposed DAS technique. The absorption spectra are used in a simplified plume model to estimate measurable concentrations for two given configurations. The plume model will also be used to evaluate field data from this initial technology demonstration as an attempt to physically quantify detection limits and other post-processing algorithms.

Species-specific detection of small hydrocarbons ($<C_{10}$) is very challenging as the absorption spectra are very similar and broad in the regions where their absorption is strong enough for simple detection methods. This is due to the hydrocarbons having a shared C-H stretch vibration that is found in the infrared. While many techniques, such as CEAS and TDLAS, scan

laser wavelengths over a features, most lasers cannot fully scan over these broad features. For the present application, the speciation of different hydrocarbons is less important than differentiation of emitted species from ambient species (atmospheric background). The DAS measurements will be path integrated at a single location without a background measurement. By identifying a region in wavenumber (or wavelength) space where concentrations of ambient species minimally interfere with the hydrocarbons of interest, we can choose an appropriate laser for DAS. The database used for the hydrocarbon spectra is from Pacific Northwest National Laboratory's (PNNL) spectral library[46]. HITRAN[47] was also used for initial comparison with interfering species.

2.2.1 Selection of Spectral Region

Findings from the studies in Chapter 1, especially the EPA Ponds study and Garfield study, have helped determine that most species of interest exhibit absorption features in the C-H stretch spectral region around 3000 cm^{-1}. Figure 6 below shows NMVOC absorption bands for species from the EPA Ponds Study. The species in blue, n-butane and n-octane, were used as representatives in their analysis of alkanes (excluding CH_4, ethane and propane) in the OP-FTIR measurements as it was too difficult to determine each species with such similar absorption features. It was assumed that the petroleum fuel-based emissions can be approximated with those two constituents.

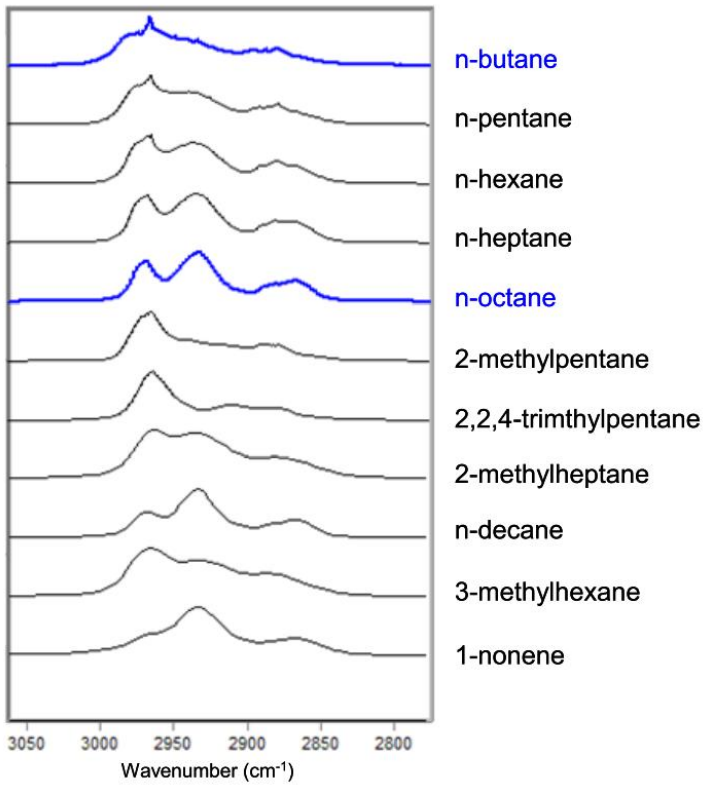

Figure 6: Comparison of the absorption bands of several species in the C-H stretch region[28].

This spectral region is plotted below (Figure 7) in wavelength for the concentrations of the EPA Ponds Study with spectra from the PNNL database[46]. This region presents significant potential for using low-sensitivity methods as the absorption is so strong even at low concentrations. It is important to note the region is very wide in wavelength (~200 nm). The species considered for this initial development include some of the highest emitted NMVOCs from each study. As was noted in Chapter 1, this will primarily include alkanes.

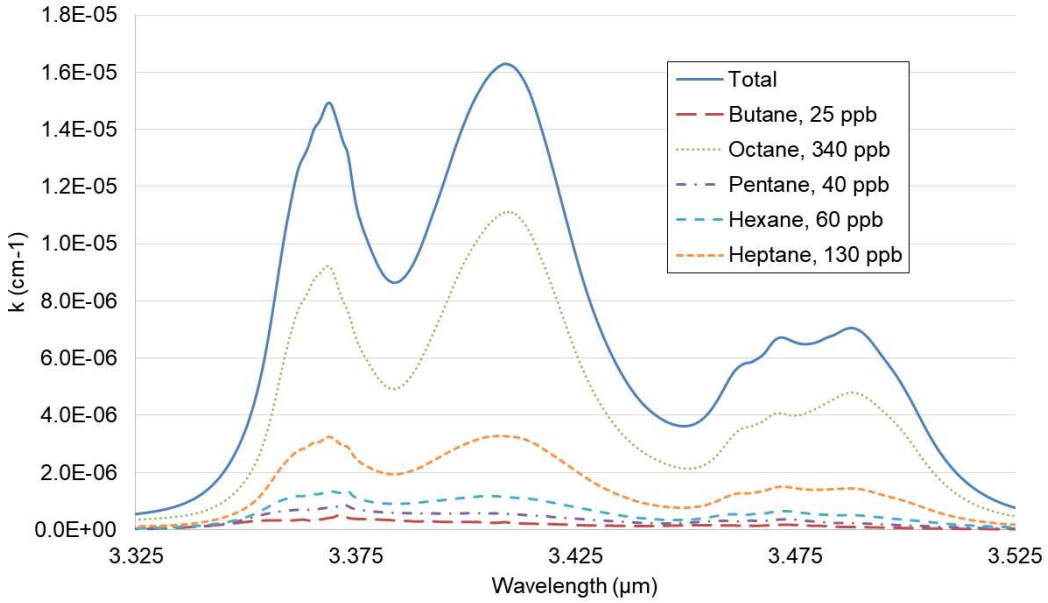

Figure 7: Absorption coefficients at EPA Pond Study mixing ratios in the 3.3 µm range.

In the mid-infrared, potential interfering ambient species include H_2O, NO_2, and CH_4 (if only interested in NMVOCs). Carbon dioxide, ozone, nitrous oxide, carbon monoxide, oxygen, nitric oxide, sulfur dioxide, ammonia, hydrogen chloride, formaldehyde, nitrogen, acetylene, and ethane at ambient concentrations were also compared at these wavelengths and showed negligible absorption (interference). Therefore, the candidate region (~3.3-3.5 µm) was analyzed to find a wavelength that would be devoid of absorption from these species, but still have strong absorption from NMVOCs. Two examples of possible laser wavelengths, ~3.410 µm and ~3.414 µm, have interference less than 5% of the total absorption for the given concentrations (Figure 8). The hydrocarbon mix in Figure 8 is the sum of selected species from the Garfield study and the absorption coefficient from the background species (H_2O, CH_4, NO_2) are also shown. Note these ambient molecules have stronger and sharper spectral features.

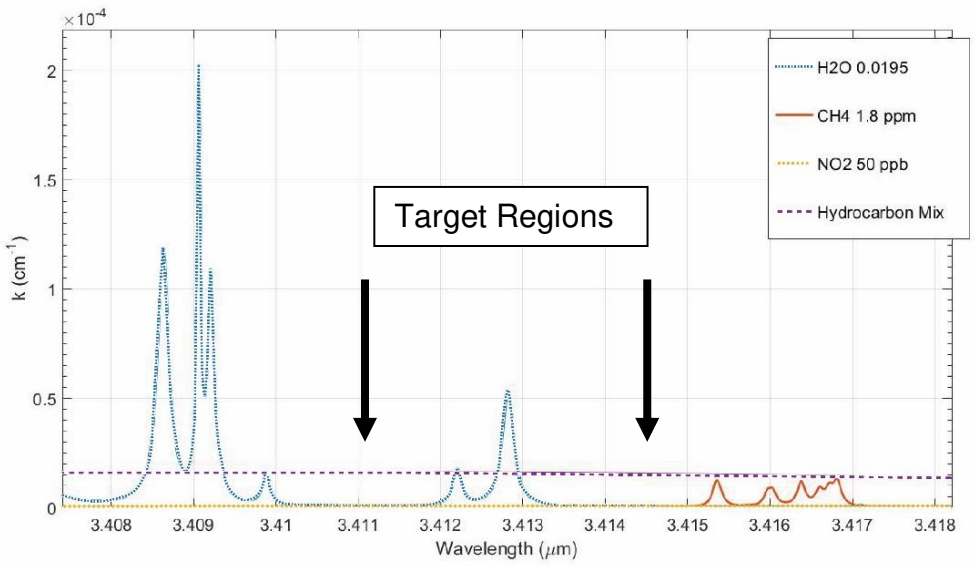

Figure 8: Spectral regions with minimal interference from ambient Species, NMVOCs from EPA Ponds Study represented as a hydrocarbon mixture.

One candidate laser was an ICL from Nanoplus, a manufacturer capable of creating ICLs at any wavelength from 3000 nm to 6000nm[48]. Generally, ICLs can be found anywhere from 2.9 µm to 5.2 µm[49]. This laser would allow for a robust detection of NMVOCs with minimal CH_4 interference. However, detecting CH_4 emissions could also be advantageous for facilities and insightful as CH_4 emissions are often accompanied by VOCs. Consequently, an infrared He:Ne was also considered as a candidate since the wavelength, 3.391 µm, has significant CH_4 absorption but is still in the spectral region relevant to VOCs.

Helium-neon (He:Ne) lasers are most commonly used for their emission at the red wavelength, 632.8 nm. However, He:Ne lasers also emit in the infrared. He:Ne lasers are gas lasers in which the gain medium is a mix of helium and neon. When the helium atoms are excited from an electric discharge, the helium is moved into excited states which then excite the neon atoms by atomic collisions between the two gases. The excited neon atoms provide population inversion in

neon and photons are emitted as the atoms drop in energy level. The 20.66 eV to 20.30 eV change in energy causes laser emission at 3.3912 µm which we employ in this application (Figure 9).

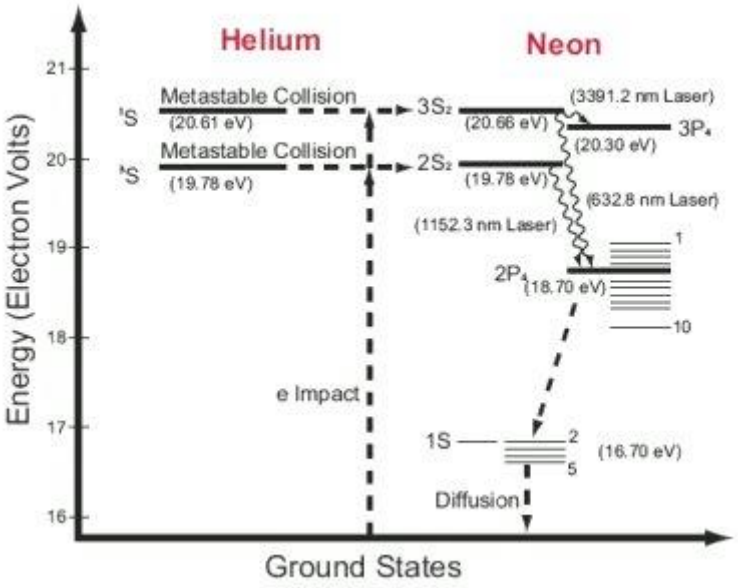

Figure 9: Helium-neon laser energy diagram[50].

The He:Ne was chosen for the first iteration of this sensor. Analysis was also performed at an ICL wavelength to explore the possibility of a non-CH_4 detection system for future applications. In addition, any issues of beam-steering and turbulent plume dispersions will be applicable for this different wavelength and laser. The He:Ne for this application was a COTS purchase from Newport Corporation which can be powered by wall power and emits two wavelengths 1.15 µm with power 2.0 mW and 3.39 µm with 3.0 mW. A shutter at the laser output allows for output of the two wavelengths or just the 3.39 µm light which aided in alignment when using an infrared card in the field.

As seen in Figure 10, the He:Ne lases at a wavelength in the region of interest (Figure 7) determined from the species and concentrations from the EPA Ponds Study. Also, the absorption by CH_4 in this region has a similar order of magnitude at ambient concentrations as the

hydrocarbons from the EPA Ponds Study. It was determined that measuring CH_4 would also better facilitate field testing as CH_4 is more readily available than a hydrocarbon mixture.

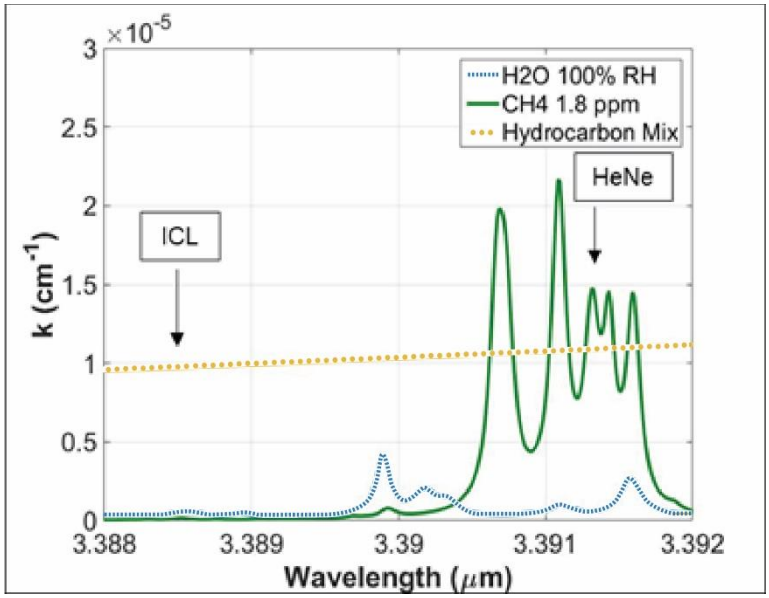

Figure 10: Comparison of absorption of an interband cascade and helium-neon lasers emissions from NMVOCs, CH_4 and water.

2.2.2 Plume Model for Emission Prediction and Validation

The role of a plume model is to link spatial concentrations to source emissions based on atmospheric transport. The model is needed for planning emissions rates to test and for interpreting sensor field data. The preliminary model is based on a simple Gaussian plume from a point stack source. To initially constrain the model, we added realistic sampling conditions similar to those from the Garfield Study. The Gaussian model is considered a screening-level model which, for air pollution dispersion modeling, is ideal for an initial estimation that tends to overestimate the instantaneous downwind concentrations[51]. It is understood that the modeled concentration can vary greatly given different ambient conditions and test configurations[52]. The following equation is used:

$$C(x,y,z) = \frac{Q}{2\pi u \sigma_y \sigma_z} \exp\left(-\frac{y^2}{2{\sigma_y}^2}\right) \exp\left(-\frac{(z-H)^2}{2{\sigma_z}^2}\right) \quad (2.4)$$

where C is the concentration in g/m^3, Q is the emission rate in g/s, u is the wind speed (assuming source emits in direction of wind) in m/s, σ_y and σ_z are mixing lengths (m) in the horizontal (lateral) and vertical direction (a function of downwind distance and atmospheric stability), y is the horizontal distance from the plume centerline (beam path for this sensor), z is the vertical distance from the plume centerline in meters, and H is the effective stack height in meters (Figure 11)[53]. The mixing lengths are derived from Pasquill stability classes and x, the distance downwind in kilometers (Appendix Table 5, Figure 43, and Figure 44) [51].

For simplicity, this model assumes that the conditions are stable and the landscape is rural. Atmospheric stability is accounted for in the mixing length calculations. Topography can have a significant change in downwind concentrations as building and natural formations can bias local weather patterns. Complex environments are challenging to model and will not be considered. Other assumptions, such as plume reflection off the ground and effective stack height from buoyancy were deemed negligible for initial research. These simplifications limit the applicability of these calculations for detection made at large distances from emissions sources. A numerical model can be used to evaluate emissions from multiple species, area sources, and account for chemical reactions. Statistical models can also be used to predict concentrations of emissions under more specific conditions.

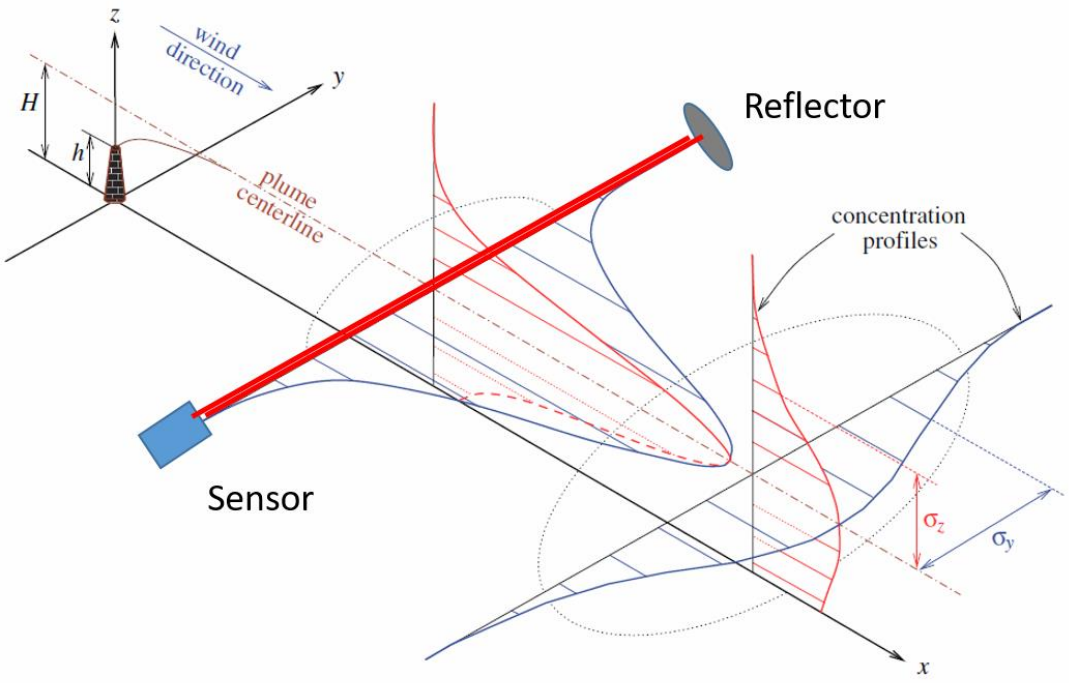

Figure 11: Diagram of physical assumptions used in initial Gaussian plume calculations (adapted from Stockie)[53].

The physical assumptions for the preliminary model which helped aid in the system design include an emission height of 2.5 m, the location of the beam at 2.5 m above ground and two cases considered with 15 m or 150 m from the source (x), wind speed of 2.6 m/s and in the direction of the plume emission (Figure 11). The dispersion of the plume is greatly affected by wind speed. Figure 12 shows the plumes as a result of wind speeds at 3, 6 and 9 m/s at a location 15 m from source with an emission rate of 2 g/s. The distance (m) on the vertical axis represents points along the beam (y in Figure 11), and the horizontal axis is the concentration (g/m^3) along the beam.

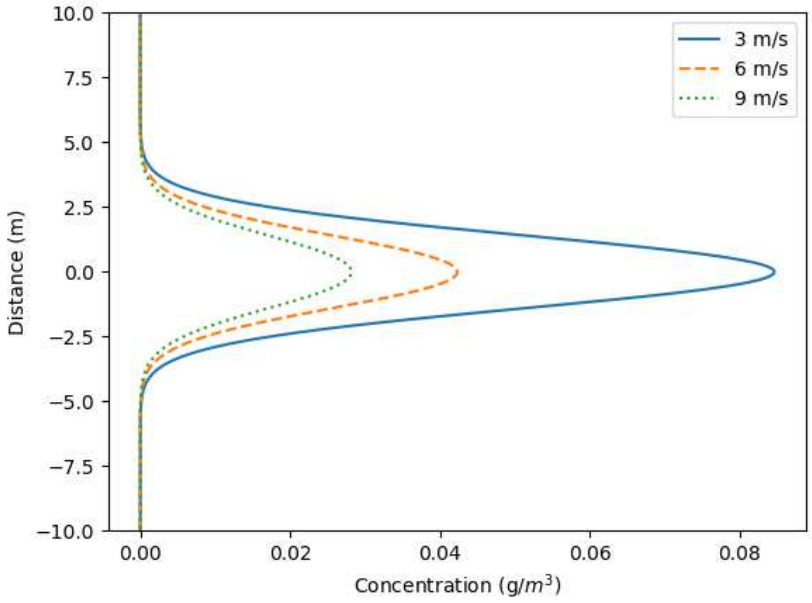

Figure 12: Gaussian plumes at with wind speeds of 3, 6, and 9 m/s along a beam 15 m from the source emitting 2 g/s.

It was also assumed for calculating absorption, that the beam will be centered on the plume with a total pathlength of 100 m with a monostatic design (laser and detector collocated with a reflector at the specified distance from the sensor). This configuration allows the beam to cross the plume twice. To simulate the path-integrated concentration as measured by the sensor along the beam, one can integrate the spatially resolved concentration along the y-direction (beam path). Equation 2.4 is integrated as a function of *y* or distance from the centerline of the plume from -50 to 50 m.

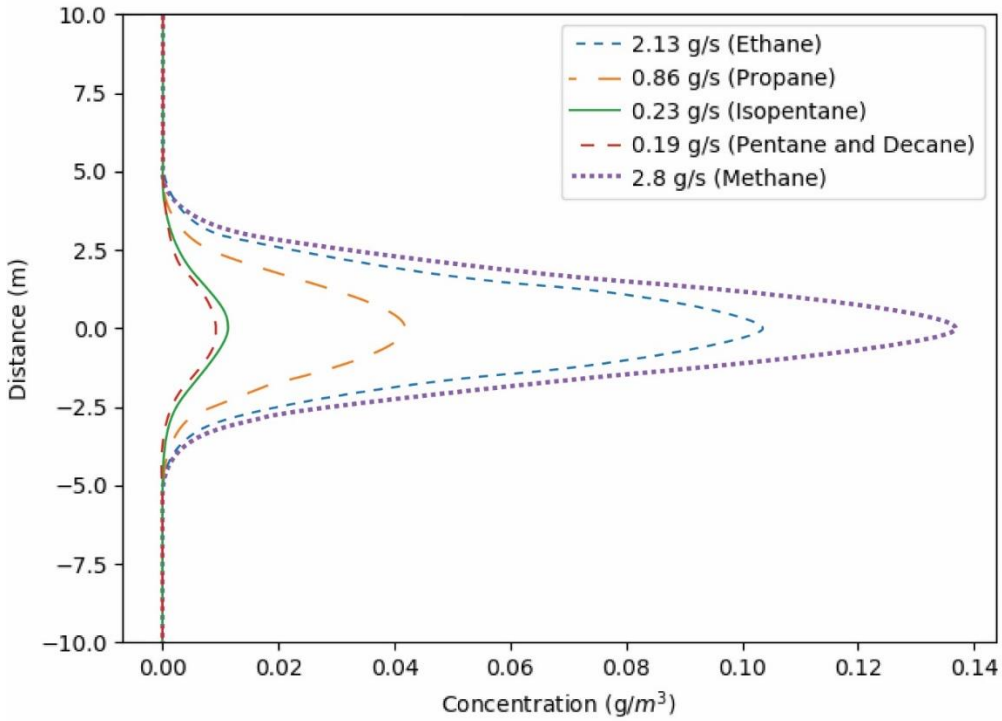

Figure 13: Gaussian representation of VOC concentrations along a pathlength 15 m from the source for given emission rates.

Figure 13 shows concentrations (g/m^3) along the beam path modeled from selected mean VOC emission rates from the Garfield Study and the mean CH_4 emission rate from hydraulic fracturing sites (chosen due to similarity to NMVOC emission rates). The mean CH_4 emission at all Garfield Study sites was 103.6 g/s with a median value of 55.8 g/s. Note that super-emitters, defined by Zavala-Araiza et al. (2017), are > 7.2 g/s of CH_4. The majority of CH_4 measurements were between 1-100 g/s[22]. It is also important to note that Figure 13 has y-axis limits of -10 to 10 m which indicates that, for this case, only a small portion of the beam is intersected by the plume for this configuration. To study feasibility of larger facility detection systems, Figure 14 shows the concentration across the beam path if the distance from the source to the sensor beam is increased to 150 m (instead of 15 m used above). This distance is a better approximation of realistic fence

line monitoring configurations. A sensor 15 m distance from the emission would need to be placed at or near the height of the emission to ensure any detection of the narrowly dispersed plume.

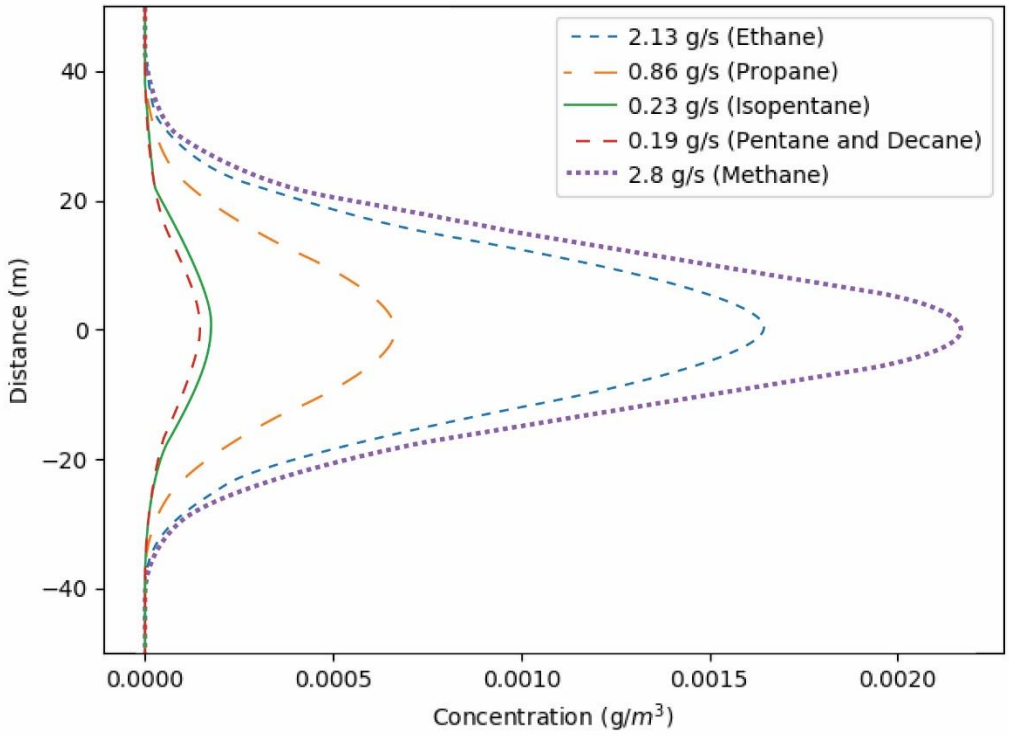

Figure 14: Gaussian representation of VOC concentrations along a pathlength 150 m from the source for given emission rates.

The modeled concentrations in Figure 14 are roughly two orders of magnitude smaller than the results from the configurations with the sensor 15 m from the source. This is not accounting for any reflection off the ground which would add approximately 0.0015 g/m^3 to the peak CH_4 concentration, for example, when calculated with methods from Sternberg et al.[51]. In this case, the dispersed concentrations span ~80 m which validated the suitability of the 100 m pathlength.

2.2.3 Detectability of NMVOCs and CH_4

The next step in modeling this technology was to analyze the laser absorption and resultant transmission for the given plume model emissions. Figure 15 shows absorption coefficients at the He:Ne wavelength for the Garfield Species, each at a concentration of 1 ppm. Figure 16 shows absorption coefficients at concentrations from the plume model. CH_4's larger concentration and strong absorption dwarf the absorption from of the NMVOCs at the He:Ne wavelength (3.391µm). Figure 17 shows the same coefficients from Figure 16 but at wavelengths in the ICL range, ~3.411 µm. CH_4 absorption at the ICL wavelength is very close to zero, and the NMVOC absorption is similar to absorption in the He:Ne wavelength range.

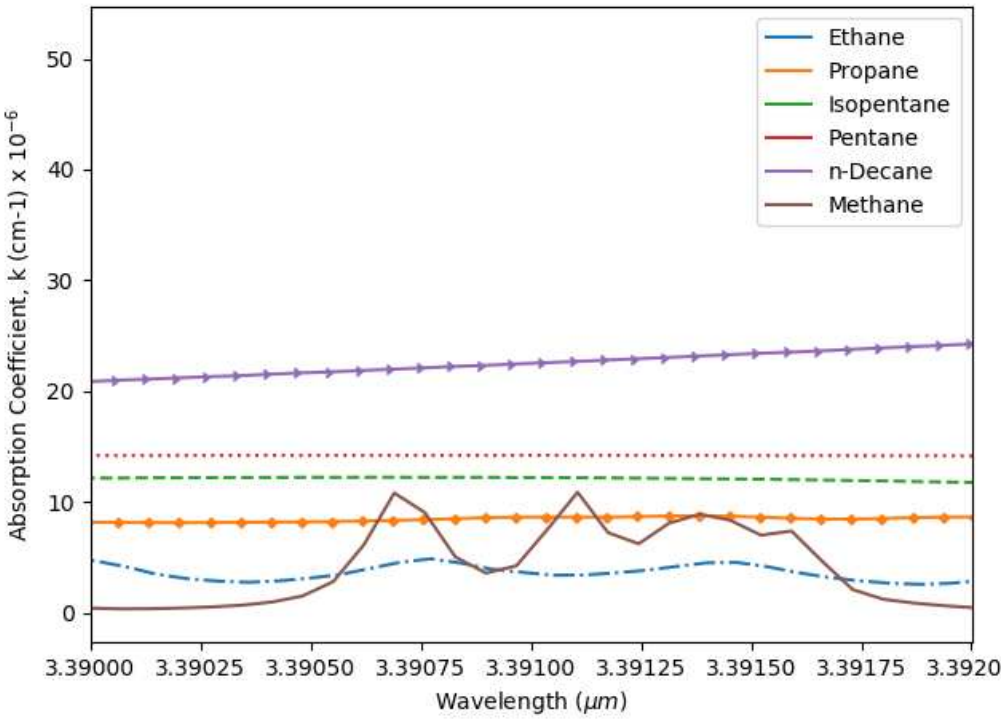

Figure 15: Absorption coefficients of hydrocarbon species at 1 ppm at He:Ne wavelength region.

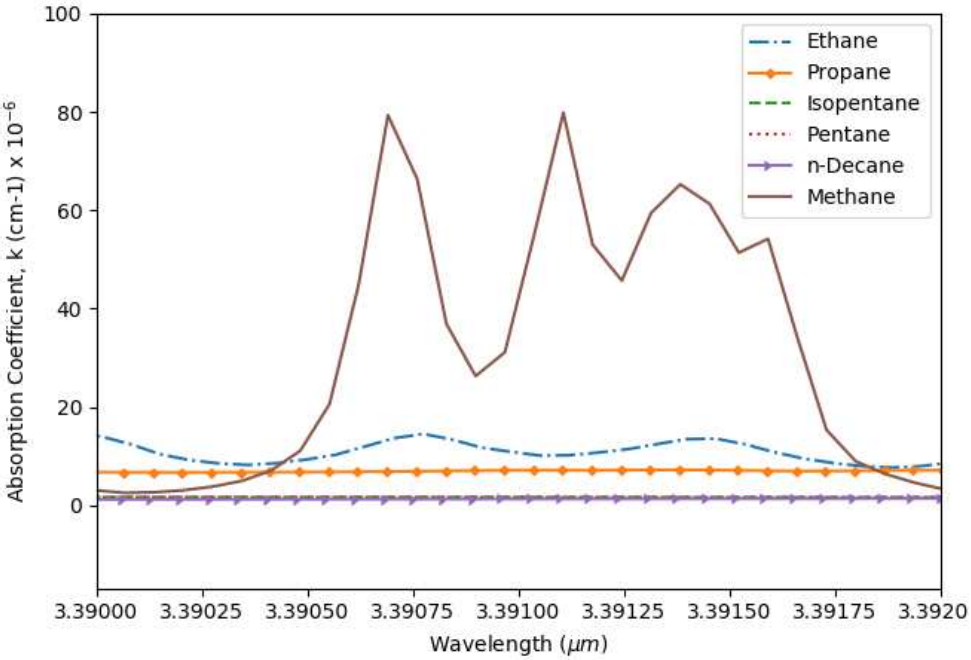

Figure 16: Absorption coefficients of hydrocarbons calculated from Gaussian plume model (15 m case) at the He:Ne wavelength range.

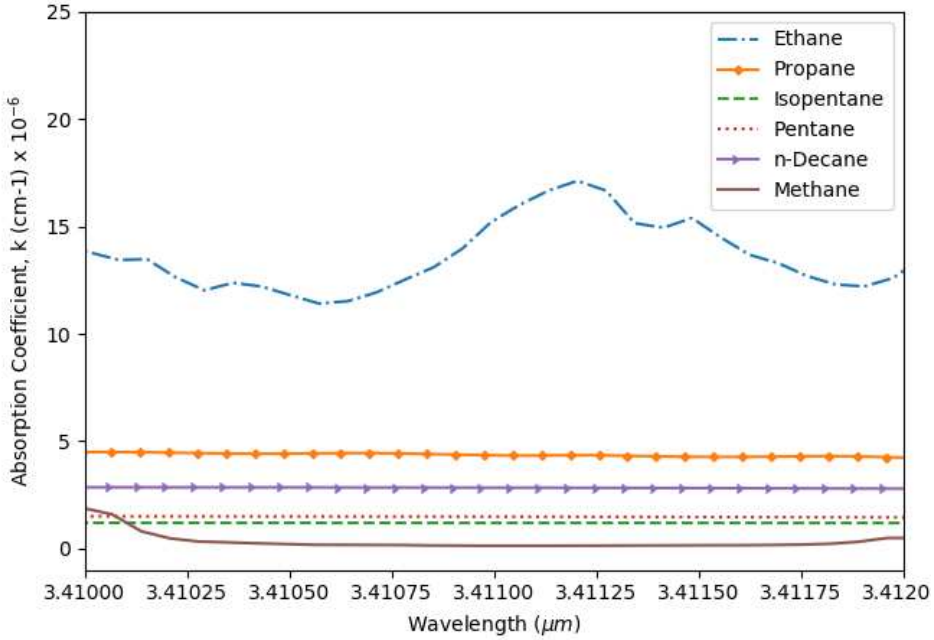

Figure 17: Absorption coefficients of hydrocarbons calculated from Gaussian plume model (15 m case) at the ICL wavelength range.

DAS has been used to measure concentrations down to parts-per-billion depending on the scheme and wavelength. Wavelength Modulation Spectroscopy, a more advanced DAS technique, is capable of measuring a ~0.1-0.01% change in signal in certain configurations (depends highly on processing and acquisition)[54]. Therefore, a change in signal of 1% or greater is ideal for detection using the proposed, simplified technique. Any super emission or larger release could also be detectable as there is still relatively strong absorption by VOCs in this region. Using calculations from Section 2.1 and the path-integrated concentrations, the transmission values as a function of emission rate were plotted below in Figure 18 and listed in Table 1. Given the assumption that ~1% change in signal is necessary, any emission rate with a transmission below 99% should be detectable, but it may be difficult to see the individual species' contributions to the change in transmission. Transmission of the ICL light for given emission rates is seen in Figure 19. Once again, CH_4, even at close proximity, causes minimal absorption.

Table 1: Path-integrated concentrations and resultant transmission for a 100 m pathlength 15 m from the source.

Species	**Emission Rate (g/s)**	**Path-Integrated Concentration (ppm-m)**	**Percent Transmission (He:Ne)**	**Percent Transmission (ICL)**
Ethane	2.13	597	80.7	73.8
Propane	0.86	164	86.8	91.7
Isopentane	0.23	26.8	96.8	97.6
Pentane	0.19	22.1	96.9	97.1
Decane	0.19	11.2	97.5	94.5
Methane	2.8	1471	34.6	99.7

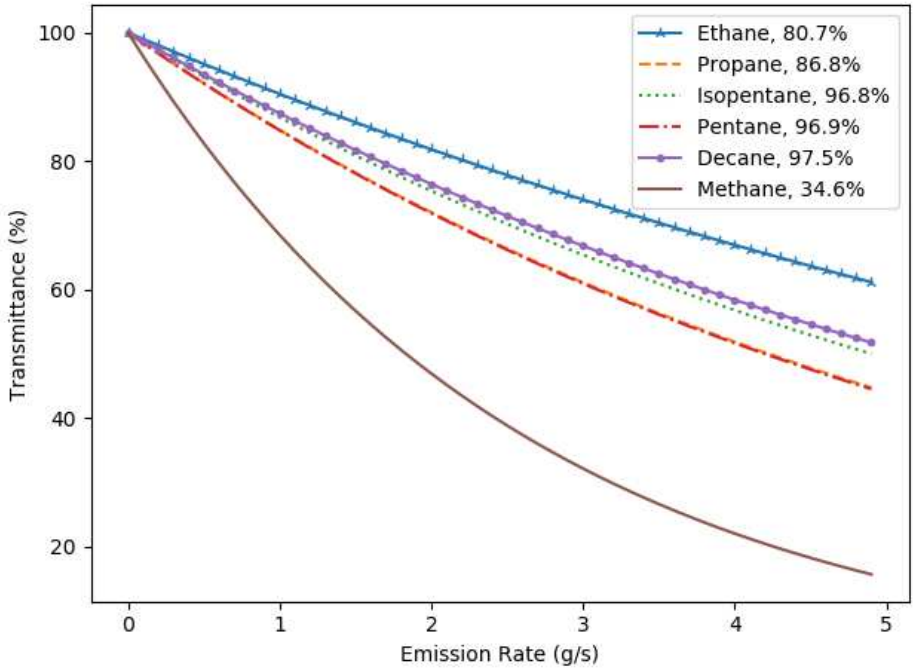

Figure 18: Transmission of He:Ne light from the Garfield Study for a 100 m pathlength, 15m from beam path.

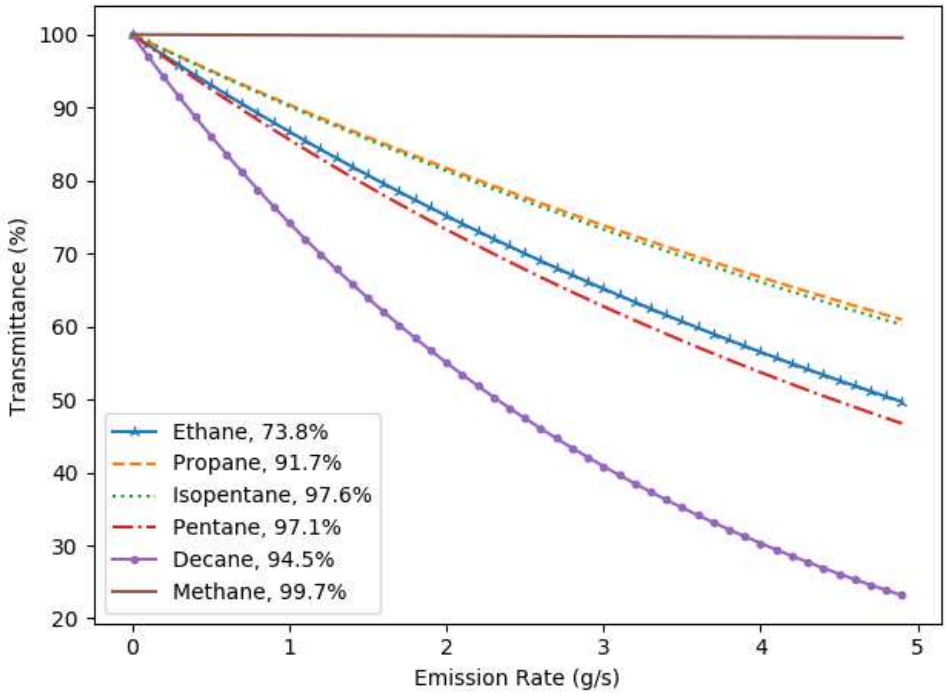

Figure 19: Transmission of ICL light from the Garfield Study for a 100 m pathlength, 15m from beam path.

This analysis predicts that DAS could be used to detect all of the analyzed emitted hydrocarbons from the Garfield study using the He:Ne or the ICL (excluding CH_4) with a beam path ~15 m from the source using a monostatic sensor. The 1% change in signal will depend greatly on the noise from the detectors and the stability of the baseline intensity detected by the system. For an optimized system, there may be the potential to detect transmission changes as low as 0.1%, i.e. a transmission of 99.9%. Table 2 also presents calculations of the transmission for each species with the sensor beam path 150 m from the source, a more realistic configuration for the final application of this sensor. Even with an increased dispersion of the plume, there would be significant drop in transmission with the use of either laser.

Table 2: Path-integrated concentrations and resultant transmission for a 100 m pathlength 150 m from the source.

Species	**Emission Rate (g/s)**	**Path-Integrated Concentration (ppm-m)**	**Percent Transmission (He:Ne)**	**Percent Transmission (ICL)**
Ethane	2.13	140.2	95.1	93.1
Propane	0.86	38.5	96.7	97.9
Isopentane	0.23	6.29	99.2	99.4
Pentane	0.19	5.2	99.3	99.3
Decane	0.19	2.64	99.4	98.7
Methane	2.8	345.6	78	99.9

The conclusion from the plume modeling is that this technique could be used for the detection of hydrocarbons emitted from oil and gas facilities. There are limitations of for He:Ne sensor pathlength due to ambient absorption, primarily due to CH_4 (~1.8 ppm), as a 150 m pathlength would have an 82% transmission of sensor light, and a 1 km pathlength would only have a 27% transmission. Therefore, when using a He:Ne source, there must be a comprise between pathlength and signal strength for a given configuration such that there is significant laser

power available to detect emissions. A 1% change and a 0.1% change are expected to become more difficult to detect with decreased transmission (signal). Using the ICL would result in less than 0.1% change in signal over 150 m (99.9% transmission) and a 0.3% change (99.7% transmission) over 1 km.

Another conclusion from this analysis is that large emissions, or super-emitter events[15], would be easily identifiable above background fluctuations. As defined in Section 1.2, 26 kg/hr (7.2 g/s) of CH_4 would be detectable by the proposed configuration (He:Ne laser) as it would result in 53% transmission if emitted 150 m from the sensor. For a given facility, emissions from nearby sources could cause slow, small fluctuations (±2 ppm) in background concentrations of absorbing species. This proposed configuration (model and test) would be able to detect this change in signal if given the correct time averaging and if the baseline is defined prior to the fluctuation. For this initial development, it is assumed that the sensor will be deployed and measuring laser intensity before a significant emission event occurs. For realistic operations, the background or baseline intensity should be adjusted periodically to account for small or slow fluctuations in background emissions.

CHAPTER 3:

Instrument Design and Validation

This chapter details the design and testing of this sensor technology which includes laboratory validation tests and optical design for the long-path field system. The closed-cell laboratory validation tests verified the absorption calculations made in the modeling, Section 2.2. The optical design required the development of adjustable telescopes to achieve long pathlengths while only using off-the-self optics and opto-mechanical parts. The built system allowed for easy alignment and redesign in the field with reasonable transportability enabling the sensor to be tested in the field by measuring controlled releases of CH_4.

3.1 CH_4 Cell Tests

This section explains the test setup and results from measuring a known concentration of CH_4 in closed cell. The lab validation of the sensor was performed using a stainless steel 62 cm flow cell with ZnSe flat windows and a bottle of 250 ppm CH_4 in parallel with the pure nitrogen. The amount of CH_4 in the ambient air before and after the flow cell were deemed negligible as more loss would come from the reflection of the ZnSe windows (29% reflectance at 3.391 μm). Light from the laser was collimated, chopped (Thorlabs MC2000) for the use of a lock-in amplifier (LIA), and steered into the cell. Both nitrogen and 250 ppm CH_4 were connected to the inlet. An outlet connected to tubing was vented into a hood. Initially, a single detector (Vigo PVI-2TE-4) was aligned with the outlet of the cell (Figure 20), and the tests were performed with a hardware (analog) LIA (EG&G, Model 5210). The chopper's reference signal and the detector signal were connected to the LIA which outputs a less noisy, amplified DC signal to be recorded by the data acquisition (DAQ) system.

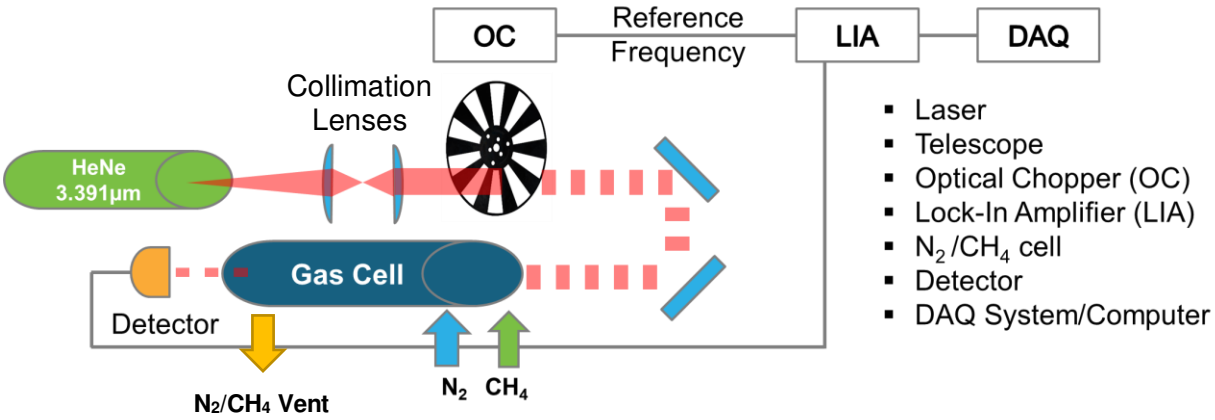

Figure 20: Gas cell lab validation test schematic.

Figure 21 is an example of one concentration ramp test where a series of concentrations filled the cell and the transmission of the He:Ne was recorded. The recorded signal without CH_4 in the cell is termed the baseline signal (I_0 in Equation 2.1 and 2.2). The expected concentration of CH_4 was calculated from the proportion of CH_4 and nitrogen flowing through the cell.

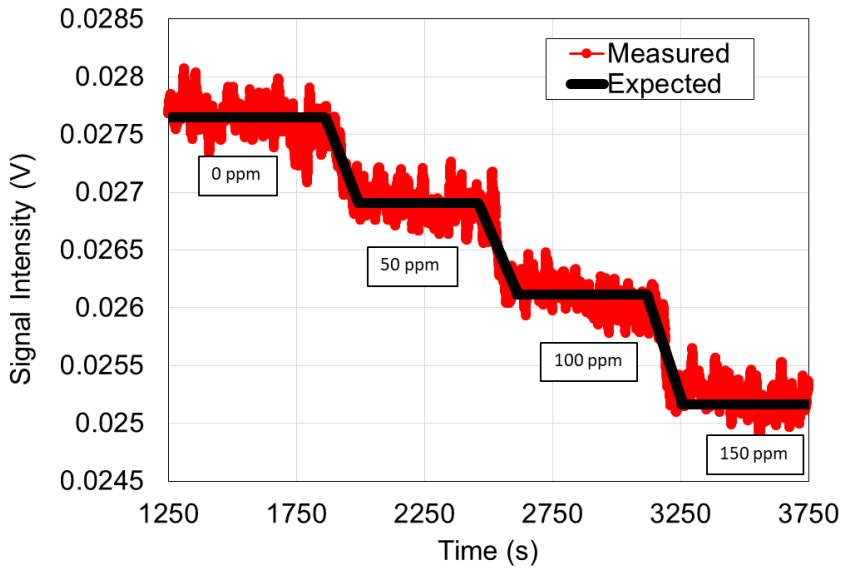

Figure 21: Example concentration ramp from closed-cell (62 cm) CH_4 measurements.

Tests varied from 5-15 min at each concentration and the non-CH_4 signals (I_0) were averaged per test for calculating each concentration value in Figure 22. Using the pathlength of the cell and the absorption coefficient at the He:Ne wavelength, the concentration of the gas sample can be calculated from the comparison of the signal without CH_4 and the signal with CH_4 present. The calculated concentration values from the experimental data are represented by measured concentration on the vertical axis and compared to the expected concentration on the horizontal axis, Figure 22.

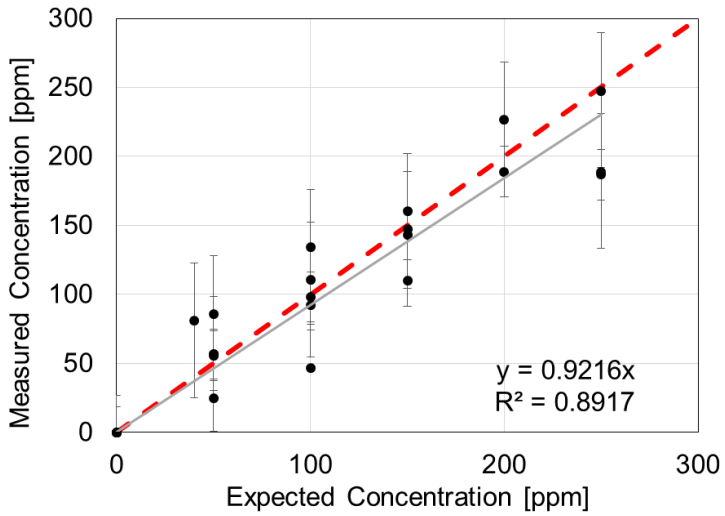

Figure 22: Comparison of measured and expected concentrations from closed-cell tests (dashed line is the 1 to 1, solid line is the linear fit). Error bars represent minimum/maximum concentrations from varying baselines.

The measured concentration values closely matched the expected values with a slope of 0.92. The fitted intercept was constrained to zero. The results are adequately represented by this linear fit with an R-squared value of 89%. To include the error induced from a variable baseline, the error bars represent the measured concentration if the minimum and maximum baseline values were used to calculate the concentration. These results, given the sources of error, imply that the proposed equipment (laser and detector) and absorption calculations were sufficient. Laser

stability and improvements to signal processing were explored within the design and testing of the field system.

3.2 Optical Design for Long-Path Field System

The goal of the optical design was to develop a system that could be used in the field to detect controlled releases with a monostatic configuration. This required low-cost, COTS optics where possible, with a large margin for adjustability and realignment in the field or between test configurations. The instrument design included the He:Ne, a transmitter, a receiver, reflector, and secondary laser for alignment. As a monostatic design, the receiver and detector are closely collocated with the transmitter and laser, and the distance between the sensor and the reflector dictates the pathlength (Figure 23). This allowed for the whole system, including a computer, to be run from a single wall outlet. Only the reflector optic was at a different location and required a tripod and adjustable mount for alignment separate from the sensor breadboard. Most trades in the final design were chosen in a similar manner to DOAS systems as outlined in Platt et al. but also with the objective of allowing for transportability and configurability[55].

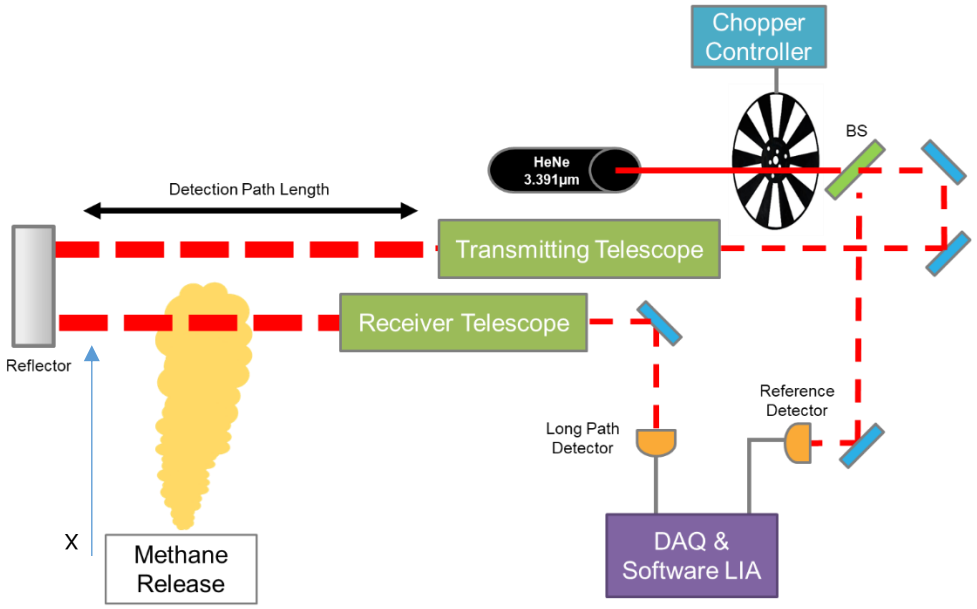

Figure 23: Schematic of controlled release test setup and sensor.

3.2.1 Telescope Design

This section details the design of the optics and support equipment required for sending light over long pathlengths. The primary task of the optical system is to transmit and receive the laser light. A cage system (Figure 24) was chosen for rigidity during transportation and to secure optics along an axis for ease of alignment. The larger optics in the cage system and the steering mirrors have adjustment for positioning the beam, but the cage fixes the height of the optics in the telescope, ensuring they are collinear. As the design is sensitive to the distance between the lenses, the cage helps make this placement repeatable and easy to adjust. In the mid-infrared, the most affordable COTS material is calcium fluoride (CaF_2), and it has ~97% transmission at 3.391 µm (depending on thickness). The major tradeoffs were between aperture size and cost.

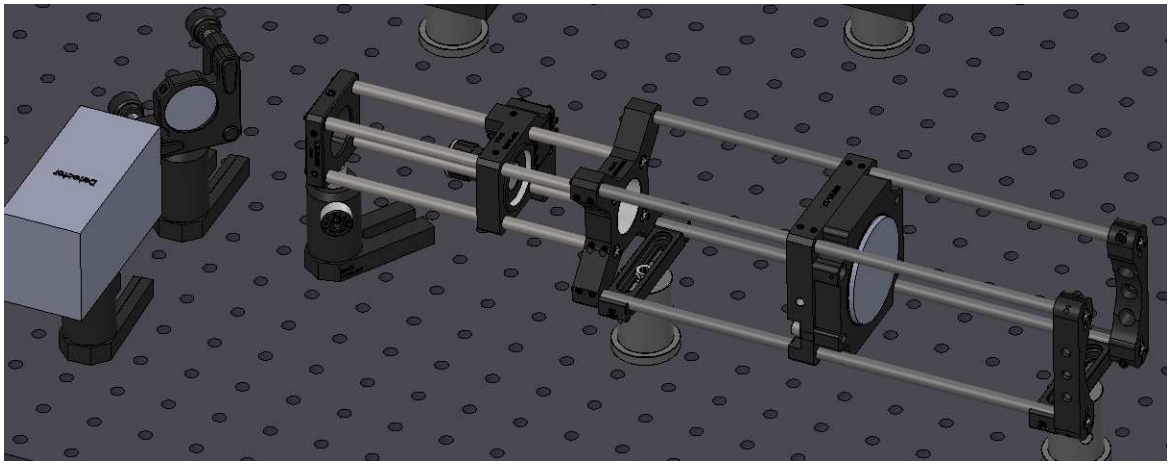

Figure 24: Model of cage system design for refractive telescope receiver.

It was determined that a design which would give the most flexibility would be two telescopes of CaF_2 lenses. A combination of focal lengths and lens diameters were chosen to maximize the Rayleigh range from available lenses using ray transfer analysis matrices[56] and the laser characteristics to calculate feasible pathlengths. The tradeoffs included sensitivity to lens spacing, overfilling the reflector, fixing on a portable breadboard, and cost. Maximizing the Rayleigh range (Equation 3.1) allowed for a longer region where the beam is approximately collimated.

$$z_R = \frac{\pi \omega_0^2}{\lambda} \tag{3.1}$$

For calculating this length, z_R is the Rayleigh range, λ is the wavelength, and ω_0 is the beam waist. The chosen lenses included 20 mm focal length, ½" diameter lenses and 150 mm focal length, 2" lenses. This combination would allow for pathlengths of ~100 m while keeping the beam size under 2" in diameter. The selected optics resulted in a beam waist of 8 mm and a Rayleigh range of ~60 m. With the monostatic design, having the reflector near the waist of the transmitted beam allows the receiver telescope to be identical, but reversed, to the transmitter optics (light collected by the 2" lens) (Figure 25).

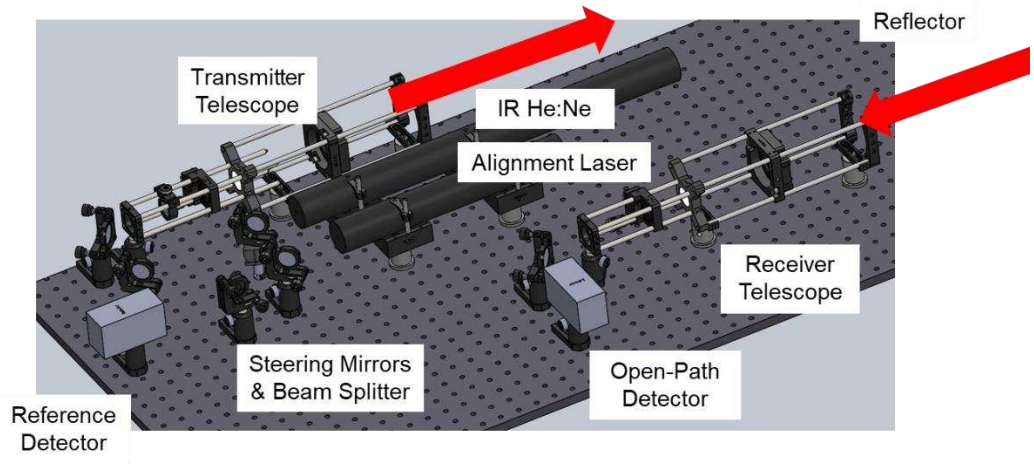

Figure 25: Field optical design with cage systems.

The effort to make a system where the beam size would not exceed 2” in the given beam path was a decision made to accommodate reflector options as well as the objective lens diameter. A simple 3” flat mirror was chosen as the reflector since the return position and angle of return would depend on the location of the reflector if the entire system was moved or adjusted. Other alternatives considered were large parabolic mirrors, corner cubes, or arrays of corner cubes. Large parabolic mirrors were excluded due to cost and availability. Corner cubes were determined the best solution for a fixed instrument, one that does not change location or need to be moved regularly. The corner cube returns light parallel to the angle of incidence with an offset dependent on the location of the incoming beam. This option would have been appropriate and ideal if the sensor’s pathlength and location were fixed. An array of corner cubes could be used if the outgoing light was expanded greatly which would be possible with a larger transmitter telescope or optics. It was ideal to choose an optical design that would allow us to use or receive as much light as possible from the laser to allow for characterization of absorption. As the pathlength of ~100 m maximum was determined from the telescope, it was concluded that the laser light needed to be reflected near but not parallel to the outgoing beam.

3.2.2 Alignment Procedure

A significant limitation with this design was the difficulty of alignment. This section explains how the system is aligned and the associated challenges. The alignment laser (Figure 25) is a green He:Ne laser at 543 nm. When expanded through the CaF_2 lenses, the green light can be difficult to see in daylight. Also, the index of refraction of 543 nm light is significantly different than that of the 3.391 μm laser through the CaF_2 lenses, yet it was necessary to have the alignment beam pass through the transmitter to optimize beam position. The largest challenge was that the infrared laser is aligned primarily with a heat-sensitive card. This can be used when the beam is smaller than ~1 cm at 5mW. It also can take over 30 seconds for the beam to become visible as the card heats up. This challenge makes the alignment of larger, weaker beams not possible. Alignment techniques dependent on thermal changes are not viable for aligning a system outside under large temperature changes. Therefore, the green laser's main purpose was to find a rough alignment of the reflector and receiver.

As mentioned, the cage system for each telescope aided in rough alignment before installing each lens by making lens positions repeatable. Two steering mirrors were used to align the beams on center of crosshairs placed in the lens holders in the cages. This configuration can be adjusted after the lenses are inserted and during the telescope alignment, but should only require fine adjustment. A flip mirror was used to switch between the green and IR beams. When the mirror is in the upright position, the IR beam is blocked and the green light is collinear with the IR beam through the remainder of the optical path.

Alignment for longer pathlengths (20 m or greater) were only possible in dark or low light conditions. If attempting to align the system in full sunlight, the beam path is very limited, e.g. 5-10 m in one direction, as the green light cannot be identified at large diameters when ambient

sunlight is also reflecting off the surface being used to trace the beam's path. The receiver telescope is position collinearly with the incoming beam from the reflector. Iterations are then made on the reflector position to capture as much of the green beam as possible in the first lens of the receiver. Finally, the flip mirror is positioned to transmit the IR beam. The detector signal is then maximized with the reflector and receiver telescope lens positions. A similar same process is done to align the reference detector with the reflected beam from the beamsplitter (ZnSe), but the alignment does not change with pathlength (reflector position) or any changes in receiver position. Ambient temperature fluctuations significantly contributed to the alignment stability and are discussed in the field test results.

3.2.3 Detectors and Data Acquisition

This section explains how the laser light is detected and analyzed. The Center for Laser Sensing and Diagnostics at Colorado State University had two detectors available in the mid-IR ranges—one centered around 5 µm (PV-2TE-5), used as the reference detector, and the other at 4µm (PV-2TE-4), used for the open-path detector, for optimal responsivity (Vigo Systems, Appendix: Figure 45, Table 7)[57]. Both detectors were deemed suitable for the main, open-path and reference signal detection and are made of mercury cadmium telluride (HgCdTe) photodiodes which is common for this range. Both use a thermal electric cooler and preamplifier to control the temperature of the diode to have a consistent response to incident light. The open-path detector's active area is 1 x 1 mm^2 and the reference detector has a 0.25 x 0.25 mm^2 area. Off-axis parabolic mirrors (OAPs) were used to focus the collimated light onto the active area. The reference detector did not need alignment after its initial positioning with the alignment of the first telescope as mentioned in the previous section. The open-path detector needed to be repositioned after each

deployment of the sensor and as the incoming angle (beam from the reflector to the receiver) changed with each position.

The uncoated, ZnSe wedged window (beamsplitter in Figure 23, Figure 25) used to pick off a small percentage (29%) of light for the reference signal was used to normalize the open-path signal to any laser power fluctuations. This reference signal, using the second detector (PV-2TE-5), will not be influenced by any controlled releases. This detector also ultimately helped identify misalignment in the system during field testing as will be discussed in Chapter 4. Ideally, a true reference detector would have the same properties as the main detector such that the linear responses are proportional and the division of the two signals should result in a signal uninfluenced by power fluctuations from the source. Figure 26 shows an example of using the ratio of the open-path (CH_4 cell for this test) and the reference detector signal to minimize the slow increase in signal and some higher frequency oscillations as the laser warms up. CH_4 was introduced into the cell around 1000 s, and the drop is more evident in the ratio signal.

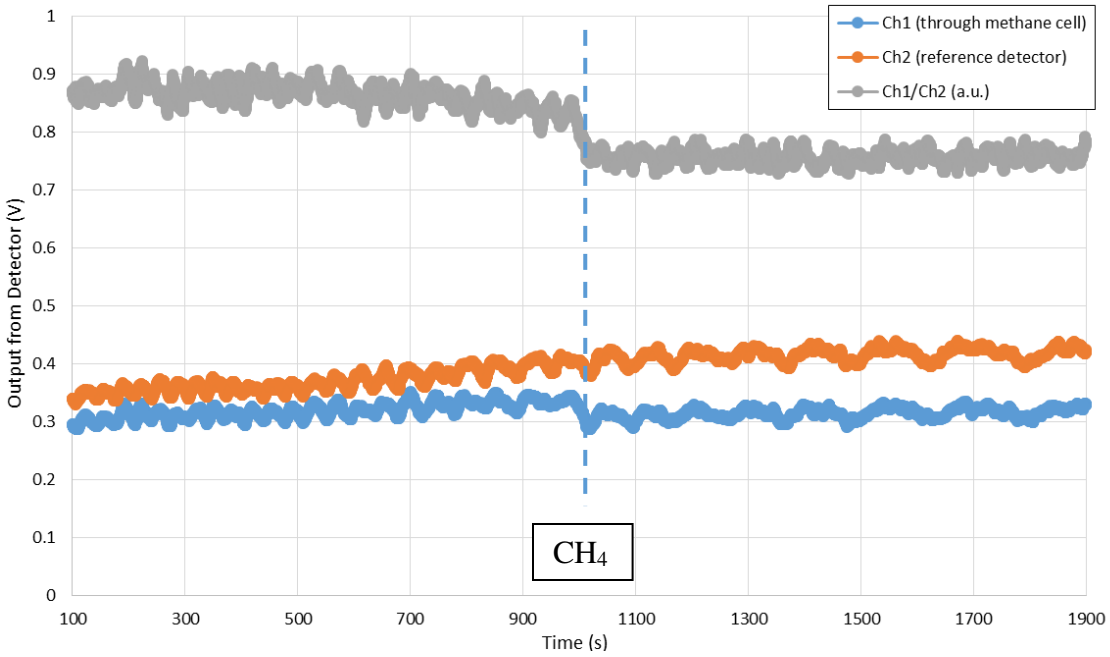

Figure 26: Laser intensity drift during warm up for closed-cell test, ratio of signals (highest signal), reference signal (middle), and the CH_4 cell signal (lowest).

Both detector signals were recorded with a COTS data acquisition (DAQ) system from National Instruments (USB-6000) that allowed for flexibility in all test configurations with the use of LabVIEW software. For this work, desktop computers with Windows operating systems were available and facilitated the use of such a low-cost DAQ system. The DAQ system included analog to digital converters for processing the detector outputs. Custom LabVIEW software was used to record outputs with a graphical display which assisted in alignment and troubleshooting of the optical system with the ability to monitor detector outputs in real time as well as some real-time averaging and filtering. The USB-6000 had a 12-bit resolution which was sufficient for detecting small changes in signal. However, there were some limitations with using a low cost DAQ system such as sampling rates and number of input channels. These limitations gave motivation for maximizing the input signal to the DAQ such that the bit noise would not mask the change in signal from absorption. Beyond raw sampling, signal modulation, a digital LIA, and averaging techniques were tested to verify the system performance. Depending on the system used, different

levels of data quality were produced. Raw data is considered to be the measured voltages from the detector.

3.2.4 Development of a Digital Lock-In Amplifier

For the DAS system to be able to detect small changes in signal, it is necessary to have a stable baseline signal with little variation. This section explains the functionality of a lock-in amplifier and the justification of its employment, followed by design details of the digital lock-in amplifier created for this sensor. As stated in Section 2.1, phase-sensitive detection (PSD) methods are commonly used in sensor systems for isolating very small signals of interest in the presence of large noise sources. A common implementation of PSD in an optical system is with a lock-in amplifier (LIA)[58–60]. A schematic of the general functionality of a LIA is depicted in Figure 27.

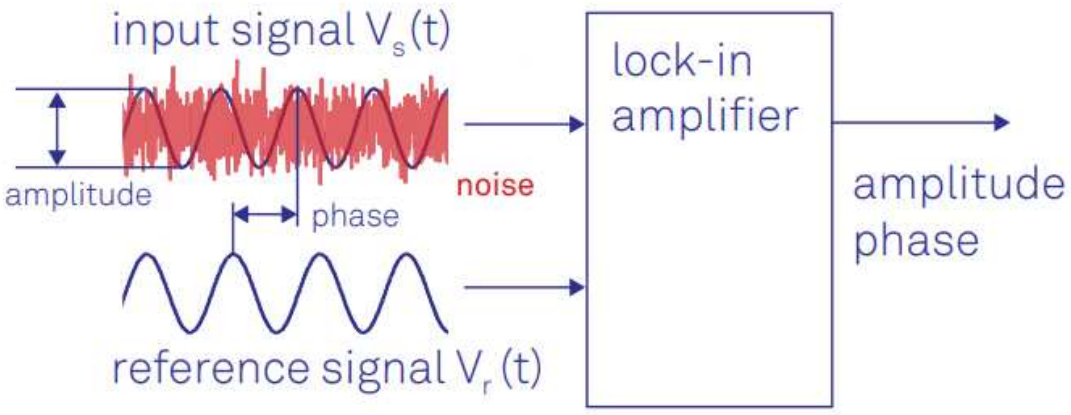

Figure 27: Lock-in amplifiers are capable of measuring the amplitude and the phase of a signal relative to a defined reference signal, even if the signal is buried in noise[61].

Hardware-based LIAs were used in the closed-cell laboratory testing but not for the field testing of this instrument. While hardware LIAs provide a sufficiently stabilized output for the DAS application, the relatively large and heavy systems (~1.5’ x 2’ x 6”, 40 lbs) do not align well

with the goal of producing a semi-portable field instrument. Therefore, it was determined that a digital or software LIA should be designed for the portable system.

A block diagram can be seen in Figure 28 that shows the steps required to obtain a LIA output[62]. This method requires modulating (chopping) the laser beam at a known frequency, creating a waveform with a specific amplitude and phase ($V_i(t)$) [61]. Upon detection of the transmitted beam to the LIA, $V_i(t)$ is multiplied by two reference signals ($V_{R1}(t)$, $V_{R2}(t)$) of the same frequency but with different phases, each shifted by 90 degrees (quadrature). The products of the signals are filtered by a low-pass filter to maintain their DC components[61]. Then these two outputs (in-phase and quadrature) are used to calculate the signal's amplitude (Vi). The LIA output is a DC signal proportional to the signal of interest, and the low-pass filters determine the output response time to input signal by the chosen cutoff frequency.

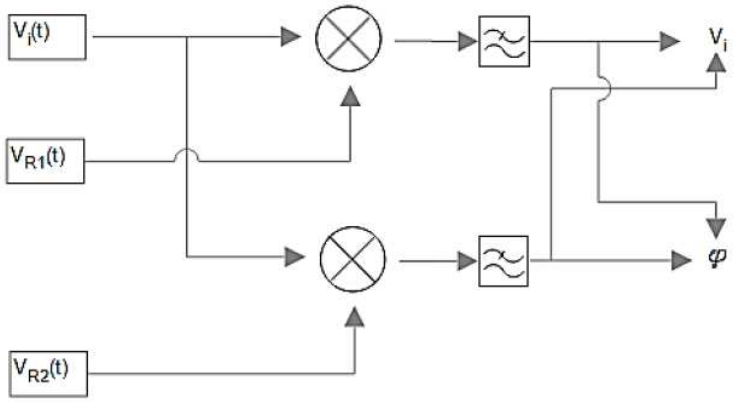

Figure 28: Block diagram of a lock-amplifier[62].

LIAs (Models, EG&G 5210), one for each detector, were used in the laboratory closed-cell tests for comparison before the development of a digital lock-in amplifier. The setup in Figure 29 shows the use of the mechanical chopper which modulated the signal and provided a reference signal to the two LIAs which both processed the analog outputs of two photodiodes detecting the laser light. Using the hardware lock-in amplifiers, it was possible to maintain a coefficient of

variation (CV), or standard deviation normalized by the dataset mean, of ~0.2% for a 1 hour when used for the closed-cell (main) signal. The CV of the reference signal was slightly lower (~0.1%) over shorter periods (1-10 s), but was similar to the closed-cell detector signal when measured over an hour.

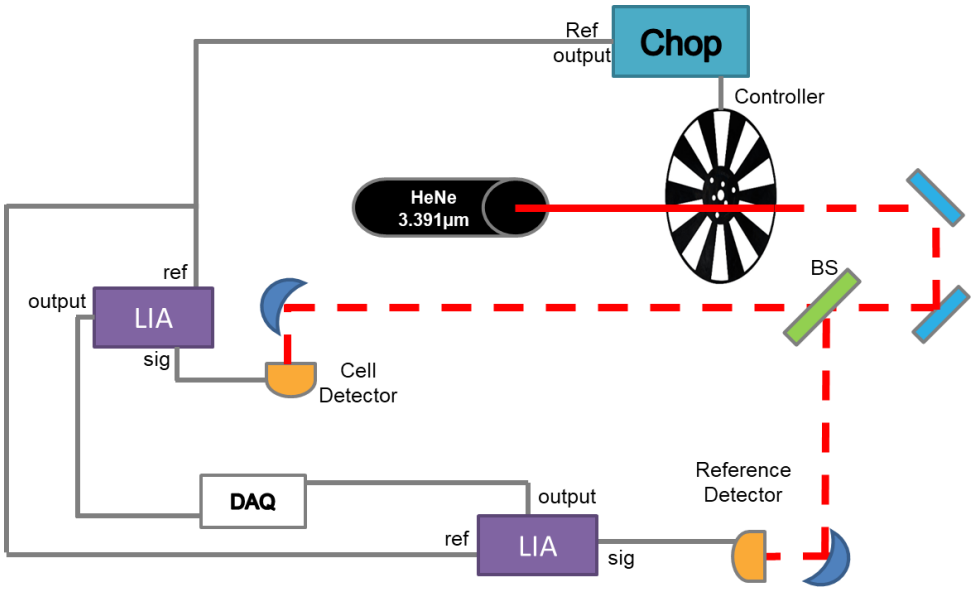

Figure 29: Diagram of two hardware lock-in amplifiers and detectors.

A software-based LIA was created in LabVIEW for the field sensor (Figure 30). It was determined that the reference signals (sine waves) created in the software could be used instead of the output from chopper controller, eliminating a cable from the system and decreasing the number of signals read into the DAQ. The analog signals from the photodiodes, digitized by the DAQ, are read into LabVIEW, split, and multiplied by two reference signals (sine waves with phases offset by 90 degrees at the same frequency as the chopper input signal at 100 Hz). The two products are then passed through low-pass filters (0.2 Hz cutoff frequency) before converted to a DC amplitude by the root-sum-square of the two signals. Parameters are adjustable in the field and can be changed during operation with the LabVIEW interface.

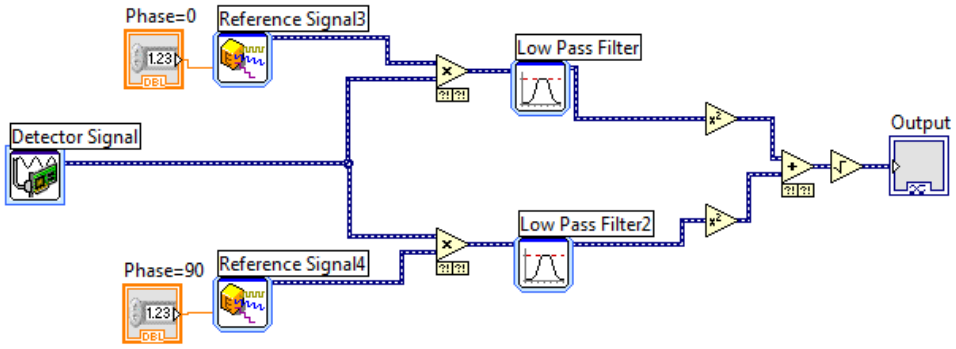

Figure 30: Simplified custom LabVIEW code for digital lock-in amplifier created for field sensor.

The software LIA is used simultaneously on the signals from the two photodiodes (open-path detector and reference detector) and is also capable of saving the raw signals and signals after amplification for post processing and analysis. The software LIA was able to stabilize the signal CV to ~1% which is close to an order of magnitude inferior compared to the hardware LIA, but still an improvement from the raw signal (no LIA), typically only able to be stabilized with CV of ~2% for these tests. Software LIA functionality could be improved with a more sophisticated DAQ system allowing for more samples per period of the modulated input signal. Nonetheless, the employment of a digital LIA significantly reduces the amount of noise in the conditioned signal while substantially reducing the amount and cost of equipment required for the portable sensor.

CHAPTER 4: Field Testing Results

This chapter uses the optical design and spectral simulation results to inform field tests of the sensor. Details of the portable field system design are explained. This includes findings from the field tests that aided in improving the stability of the instrument response. The results from two datasets of controlled release tests are presented.

4.1 Proof-of-Concept Portable Field System

An initial breadboard system to be used outside of a laboratory setting was a step towards a ruggedized, portable instrument. A custom cart (Figure 31) with a 65 x 26" breadboard was made to deploy, transport, and store the sensor. This cart was built primarily from 80/20 with a lower shelf for a computer and monitor. Casters with adjustable heights and plastic pads were used for vibration dampening and course alignment of the system. The breadboard is a COTS item which is slightly oversized for the optical design, but allowed for rearrangement and experimentation. The optical breadboard was large enough to accommodate both the transmitter and receiver telescopes, two detectors, two lasers (green He:Ne for alignment and IR He:Ne). A second computer (Figure 31) was used to record ambient temperature and humidity at the sensor location.

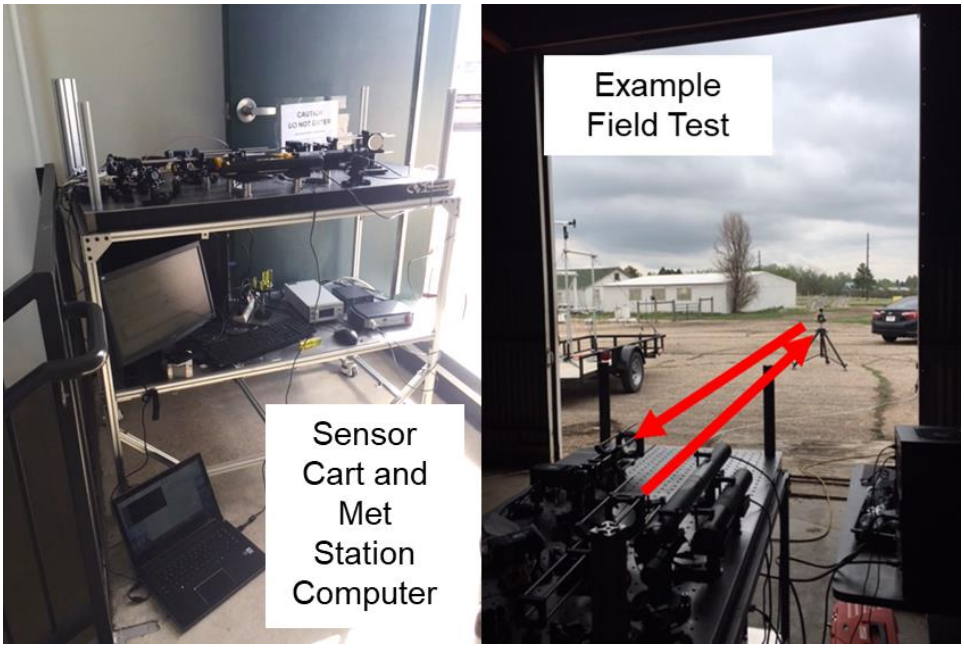

Figure 31: Mobile cart sensor and example field test setup.

The digital LIA was used on several tests, but the system was also used without the modulation of the signal primarily for ease of monitoring misalignment. A heavy tripod was used to hold the reflector (3" mirror) which was secured in an adjustable mount at a distance defining the test pathlength. The system was able to roll to a desired location that allowed for the release of CH_4 approximately perpendicular to the beam path.

4.1.1 Instrument Signal Stabilization

During the testing and the initial operation of the laser, it was demonstrated that there was significant drift in the laser power over the first hour of operation, similar to Figure 26. This phenomena in He:Ne lasers has been documented by others, and its effect can be minimized with the use of a reference detector to normalize the laser power output (Section 3.2.3)[63]. Therefore, all field tests and alignment procedures were performed after warming up the He:Ne.

To understand the stability and detection limitations, the sensor was first tested indoors with only ambient gas (no emissions) and multiple pathlengths up to 15 m. Coefficient of variation,

CV (also used in Section 3.2.4), is used as a metric for understanding the stability of the signal over different time periods and voltage ranges. CVs of the raw open-path signal (not normalized by the reference signal) in an indoor setting at 15 pathlength averaged 1.9% for an hour test with 1 kHz sampling. It was also demonstrated that a 1.1% CV is possible with the data is filtered with first-order Savitzky–Golay filter, a common method for smoothing noisy data while maintaining the ability to keep the structure of the signal[64]. This environment, while indoors, was still highly susceptible to dust and aerosols from people walking around, vibrations of the cart and the reflector as well as temperature swings. These baseline tests allowed for the development of the alignment procedure.

Stability of the baseline signal was also observed for each test environment used in the controlled releases. From these observations, it was found that the effects of wind, sun and ambient temperature could not be neglected. Long-term tests show a large instrument response to temperature and humidity changes which caused appreciable alignment degradation. A temperature controlled enclosure may be needed in this regard.

In order to quantify the effects of the environmental changes, a temperature and humidity sensor (RHT03) was connected to a microprocessor for logging measurements every 10 seconds. The sensor was placed on a plastic breadboard collocated with the optical breadboard. Wind speed was also recorded by the same microprocessor from a cup anemometer (InSpeed Vortex) located near the middle of the beam path. Figure 32 is an example of temperature, humidity, and wind speed verses signal for the tests performed outside with a 30 m pathlength. The system was insulated behind a door with a cutout for the first half of the test and then exposed to ambient conditions for the remainder of the test.

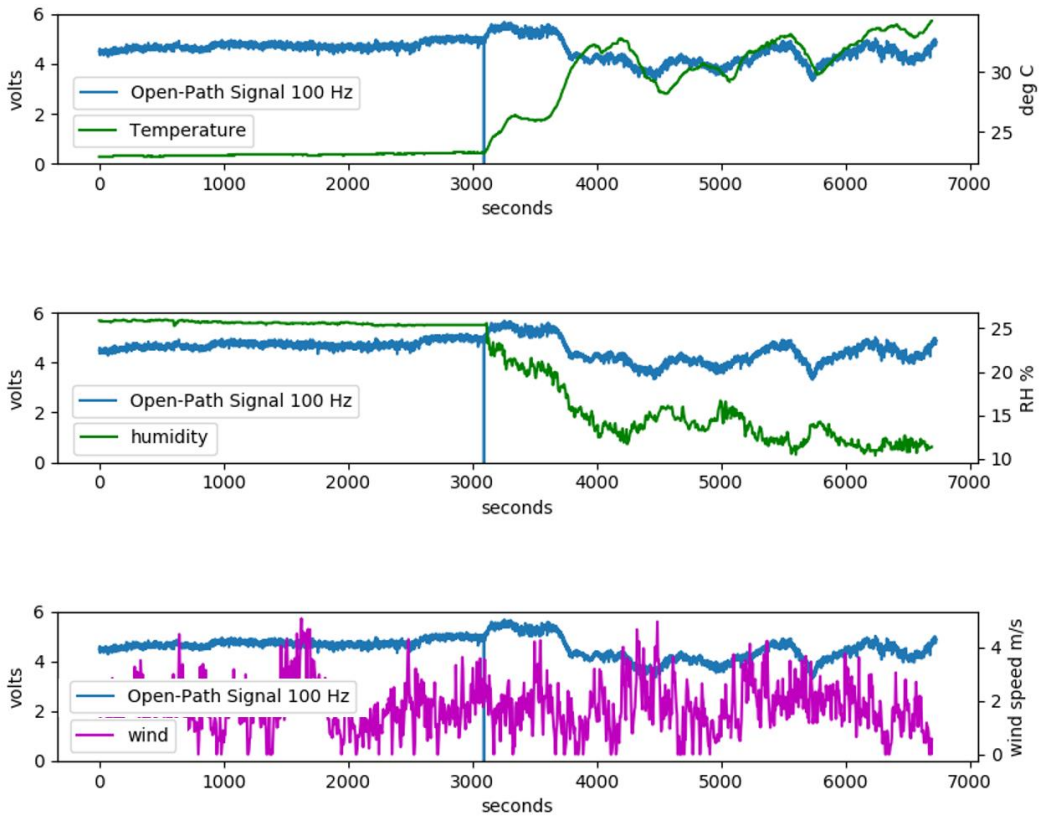

Figure 32: Open-path signal and environmental comparison for an insulated sensor (0-3000s) and exposed sensor (3000-7000s).

Given these results, tests were performed where the sensor was stored in a stairwell with a door opening to a rooftop with enough space for a ~30 m pathlength. An insulated temporary door with a cutout for the beams was installed to keep the sensor itself as isothermal as possible (Figure 33). The system, before insulated, had baseline values with a CV of ~11%, but the CV decreased to ~2% with the inclusion of the door for tests of 1 hour.

Figure 33: Sensor test location with insulated door (left) and cutout (right) for beam paths.

Using the reference detector ratio to normalize of power fluctuations was more achievable with the use of an insulated breadboard system. Figure 34 shows a dataset during warm up where atmospheric fluctuations from the open path are still apparent, but the ratio signal is flatter due to the reference signal tracking the increase in laser power. The initial dip is due to a person walking in front of the beam during the alignment process. The ratio signal is relatively flat from 2000-5000s. Long-term drift is still present but a transient plume in this signal would be visible over short periods.

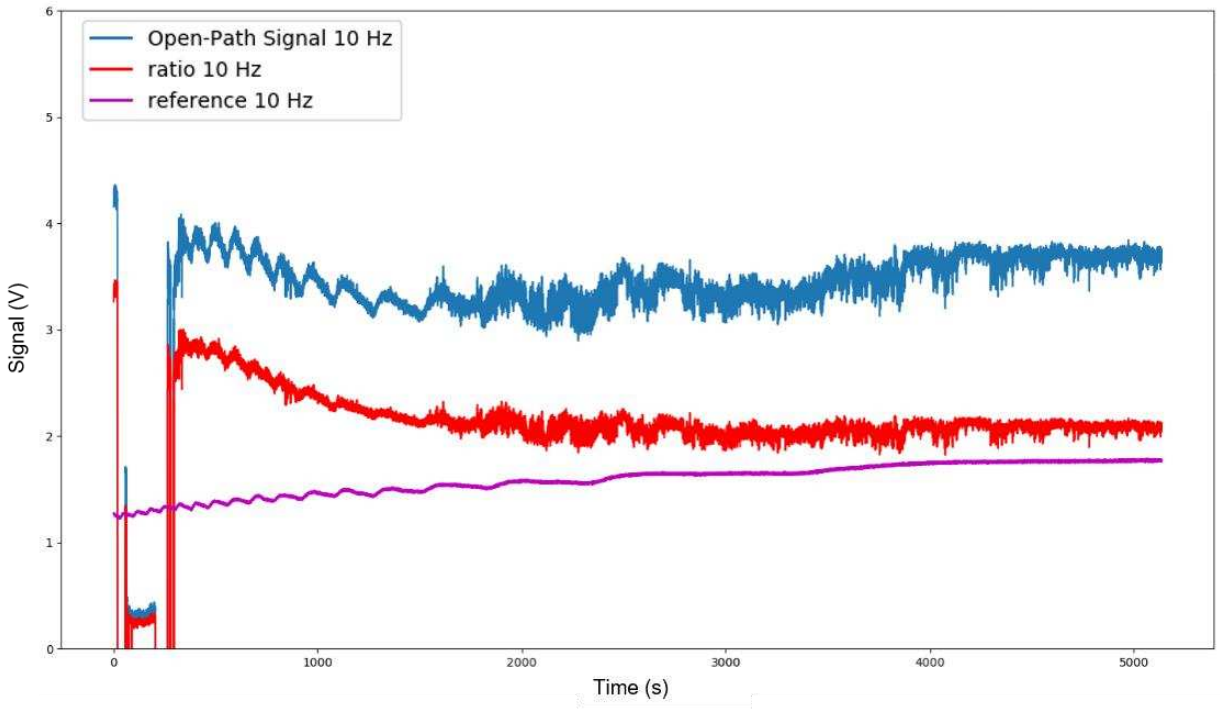

Figure 34: Reference detector signal (lowest voltage), open-path signal (highest) and the ratio for laser power normalization for insulated test setup.

4.1.2 Controlled Release Tests with Field Configuration

The primary objective of sensor testing with CH_4 releases was to gather data from a remote point source and examine predictions from the plume model. CH_4 was used as the absorber due to its strong signal and ease of availability. The typical configuration (schematic in Figure 23) for all of the field tests included a single pathlength (out and back) and the monostatic breadboard sensor design with a release source approximately perpendicular to the beam path. The height of the release was approximately at the height of the beam path (~2.5 m). The flow was monitored and adjusted using with flowmeter (0-10 L/min) near the outlet. The length of the tubing from the CH_4 bottle to the outlet was dependent on the pathlength. The lateral position of the release was located at approximately the midpoint of the beam path (one direction). The x-distance (Figure 23) between the release outlet and the beam path (~2 m in Figure 35) varied during the experiments to allow for validation of the plume model. A fan was introduced to have more consistent (effective)

wind speed and to control the direction to be approximately perpendicular to the beam path. The final application of this sensor is a fence line detection system, i.e. with the beam surrounding a facility. In this proof-of-concept, the sensor only uses one beam path. Under non-ideal wind conditions, the emission or release event can be completely undetected. Testing with just the use of ambient wind conditions was attempted at every test site but was deemed too inconsistent for the initial validation of this sensor.

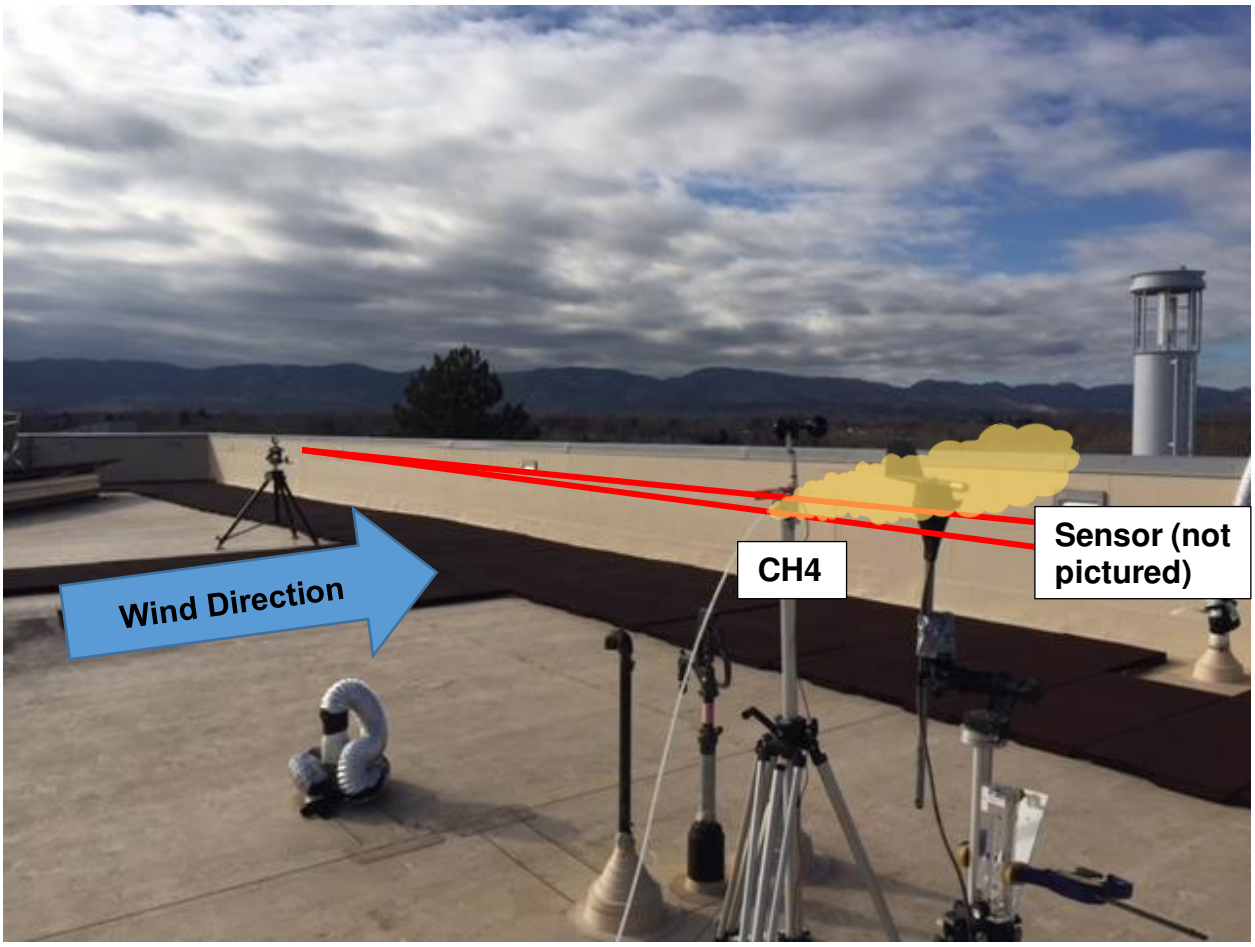

Figure 35: Field configuration for controlled release tests (sensor located right of photo in stairwell doorway).

Figure 36 shows an example of the signal ratio during a test with multiple CH_4 releases. Ambiguity between signal changes (4-8 L/min having similar responses) resulted in the decision to do preliminary testing at 2, 6 and 10 L/min to have a larger spread in emissions rates.

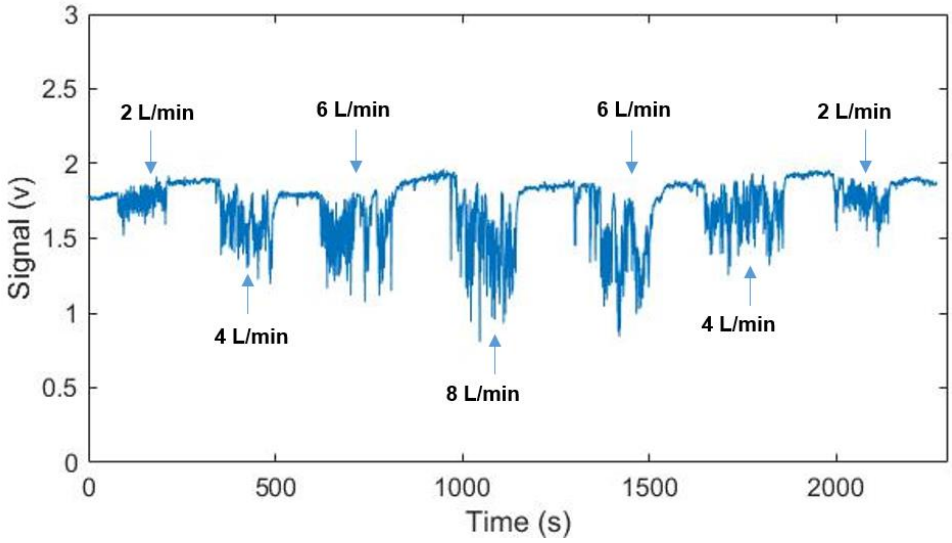

Figure 36: Initial controlled release test to determine flow rate resolution and instrument response.

The first location was on the 4th floor roof of the Powerhouse Energy Campus (40°35'37.94" N 105°04'33.45" W). This location had a significant amount of ambient exposure which made controlling wind direction difficult. Another location (40°35'39.40" N 105°04'32.40" W) on the ground floor outside of the Powerhouse was more secluded and blocked from the wind making it more suitable for initial tests. The final location, Site 4 (Figure 37) was on the 5th floor roof of the Powerhouse Energy Campus (40°35'38.92" N 105°04'32.21" W). This area had limited pathlength capabilities but allowed for repeatable release tests and reliable storage of the sensor.

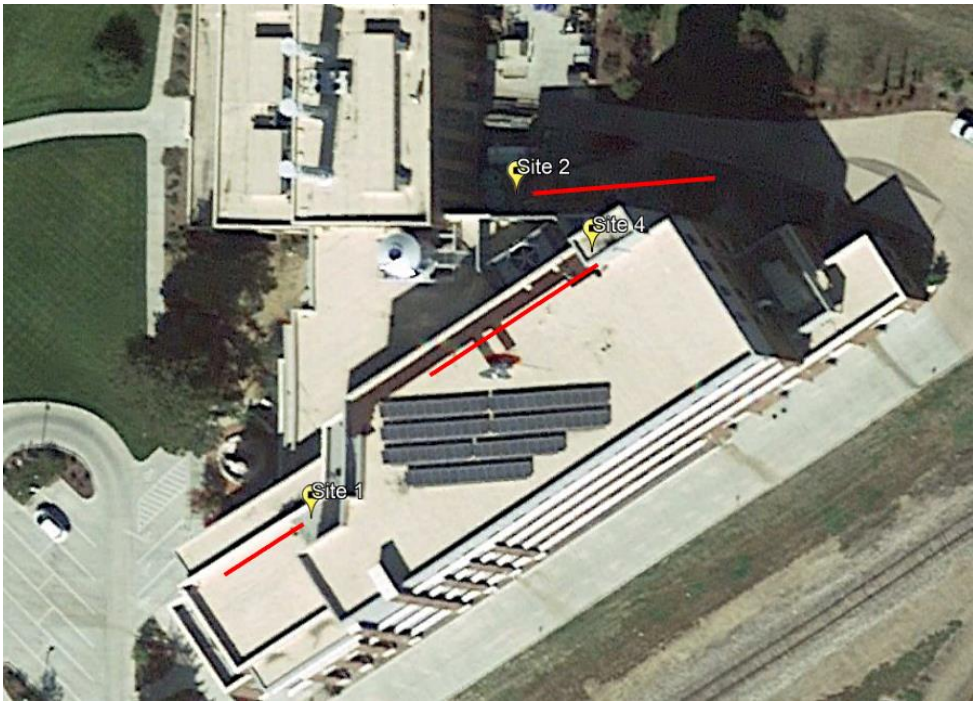

Figure 37: Google earth imagery of test sites at the Powerhouse Energy Campus.

4.2 Field Test Results

The initial field testing yielded two datasets that were compared in detail to the plume model. The first is a dataset with multiple releases at different flow rates at a single location from the beam path (5 m). The second dataset is comprised of releases at variable distances (2, 5, 10 m) from the beam path and different flow rates. The change in light intensity received by the sensor was used to calculate the absorbance for the given releases. In a similar calculation that was used in the cell tests to determine the measured concentration, Beer-Lambert's law (Equation 2.2) is used to calculate absorbance (*A)* as the metric for comparison to the expected results from the Gaussian Model.

Figure 38 is an example of a single field test with three CH_4 emissions at 2, 6, and 10 liters per minute (L/min) with the source 5 m from the beam path. The initial characterization of

emission events within ±2 L/min was challenging due to the ambiguity between instrument responses. Therefore, emission rates for initial testing were spread across a large range to be easily distinguishable. While there is some instability in the baseline values (no CH_4), it is very evident when the emissions begin and end. CH_4 was emitted for 4 minute per emission and the baselines were 4, 6, and 4 minutes in length. When taking the average values of the emission events, the calculated emission durations in this example averaged 3.8 minutes. For the baseline values, each interval varied and was averaged where the signal stabilized. Figure 38 includes a down sampled signal and a first order Savitzky-Golay filter (10 s) to better depict the significance of the drop in signal for each release.

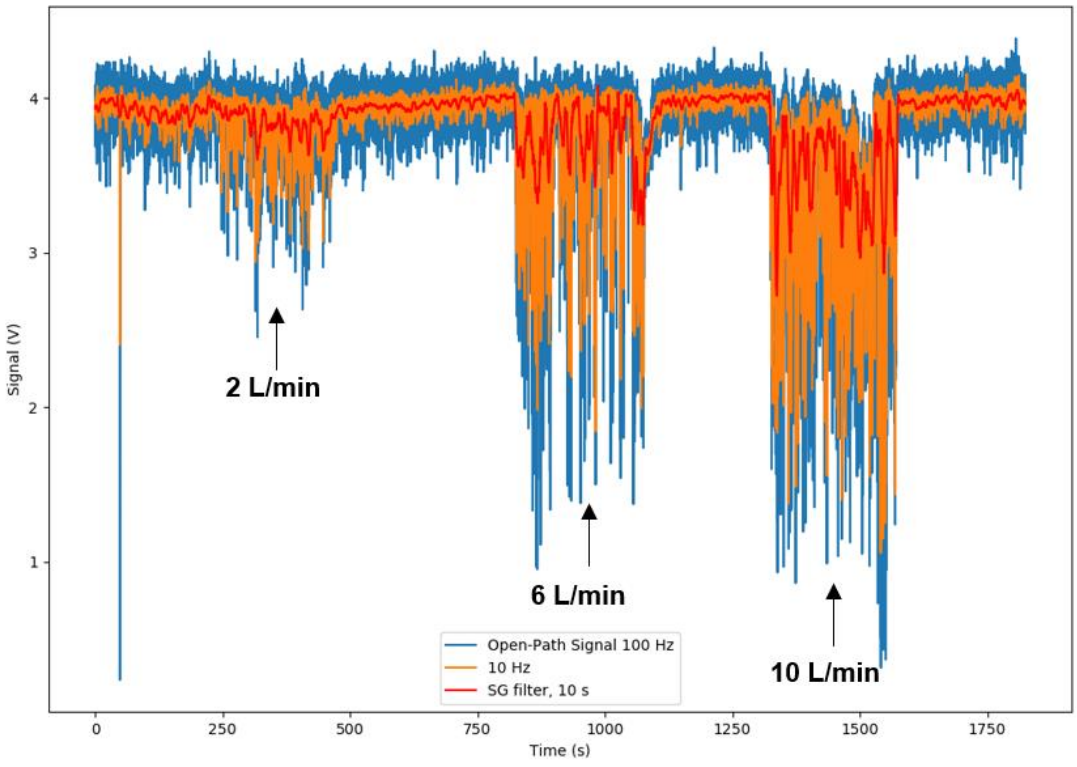

Figure 38: Example time series of controlled CH_4 release of 2L/min, 6L/min, and 10 L/min, 5 m from the beam path, down sampled to 10 Hz, and a first order Savitzky Golay filter.

The modeled absorbance (Figure 39) was calculated using the average wind speed (2.28 m/s) of all of the tests performed on 10/27/2017. The wind speed was measured locally with the cup anemometer and varied greatly throughout all the tests despite the use of the fan at a constant speed. The localized (near the emission location) wind measurement resulted in higher wind speeds compared to a nearby station at Colorado State University which averaged 1.33 m/s for the duration of this test.

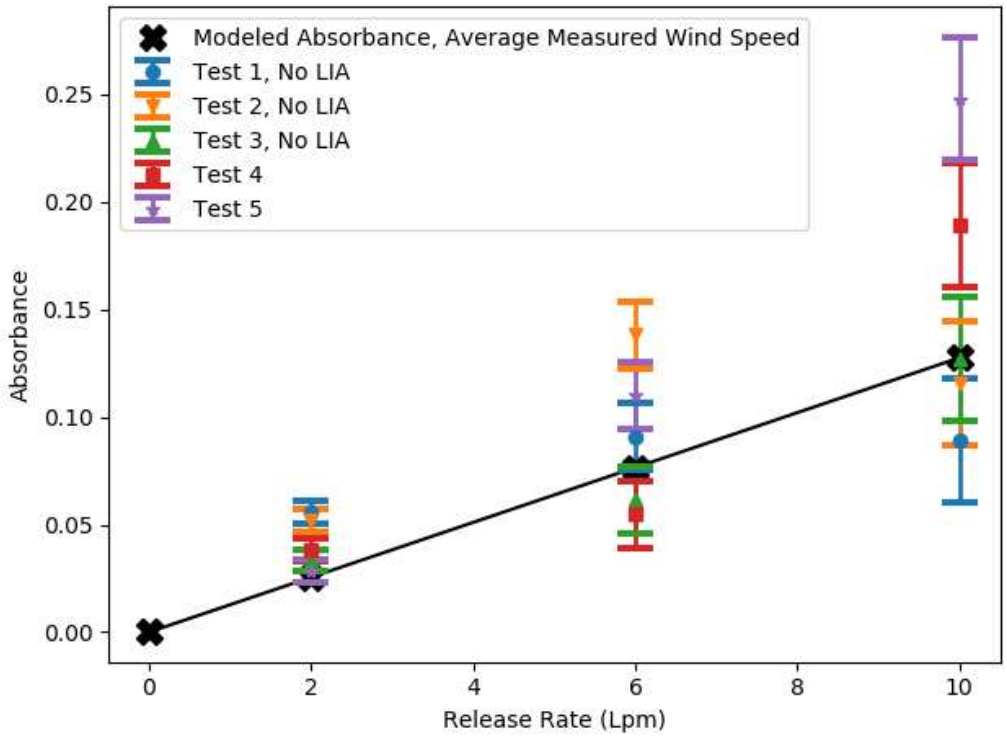

Figure 39: Release test absorbance compared to Gaussian model for given release rates at the average wind speed for the entire dataset (10/27/2017).

Figure 39 shows reasonable agreement between model predictions and measurements for this dataset. Error bars represent the variability between each emission event with the standard error of the mean for each release rate. Standard deviation of the absorbance calculation for each emission event is listed in Table 4 (Appendix) and inherently includes the variation of the baseline. CVs for the baselines were similar for each test at ~1.4%.

Figure 40 compares the expected absorbance from this dataset calculated using the plume model with the measured change in signal from the release tests. A linear fit of the data yields a slope of 0.99 with an R-squared value of 74%. The error bars represent the standard error of the mean for each measured (detected) absorbance value. The emissions with lower release rates have less variability. As was evident from Figure 38, the variation of the signal increases significantly with the increased flow rate or emission, especially without any averaging or filtering.

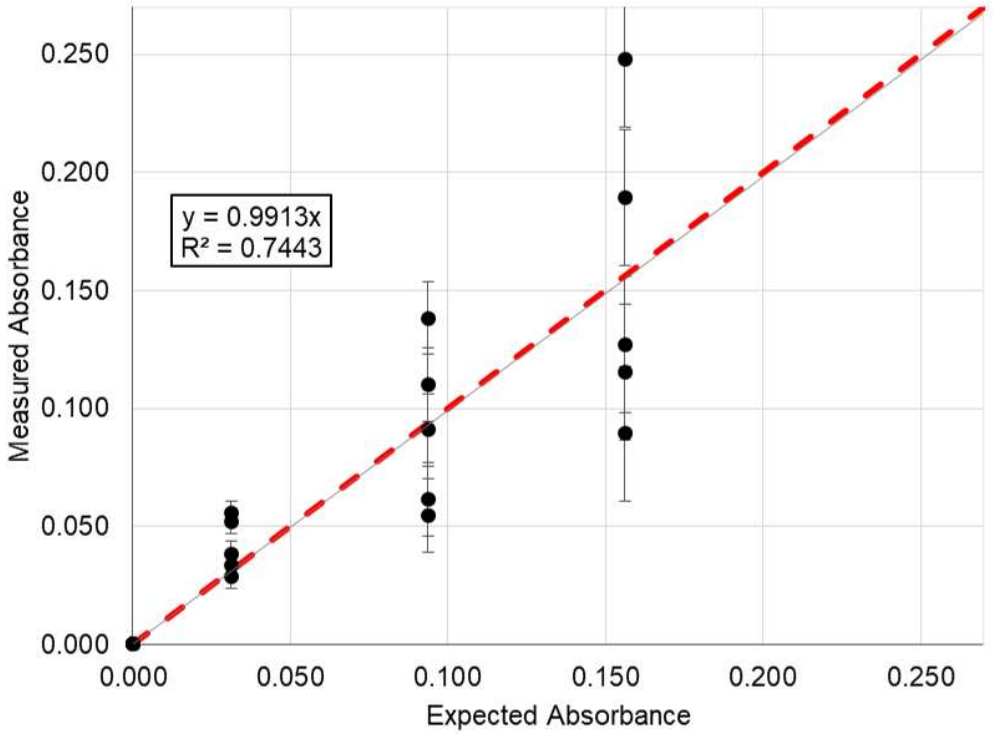

Figure 40: Measured vs expected absorbance for 10/27/2017 controlled release tests (error bars represent standard error of the mean).

The ratios of "Average Wind Model / Experimental" (Table 4) describe the factor by which the model over or under predicts the absorbance values. When averaged, the model/experiment ratio for all tests was 1.04, which, given the variation in signal, shows significant agreement. It can be assumed that the low wind speeds and short distances to the beam path allowed for such excellent agreement in absorbance values.

The next dataset was performed with the same release rates but with three different distances from the beam path to further study the effectiveness and validity of the model. The simple Gaussian plume model predicts that the concentration will be lower when detected farther from the source. This is due to the plume being increasingly dispersed in the z-direction (above and below the beam), resulting in less CH_4 in the beam path (Figure 41). It is also significant to note the width of the plume as predicted by the model. For this test setup, only a ~6 m pathlength would have been necessary to capture the entire emission at any of the given distances.

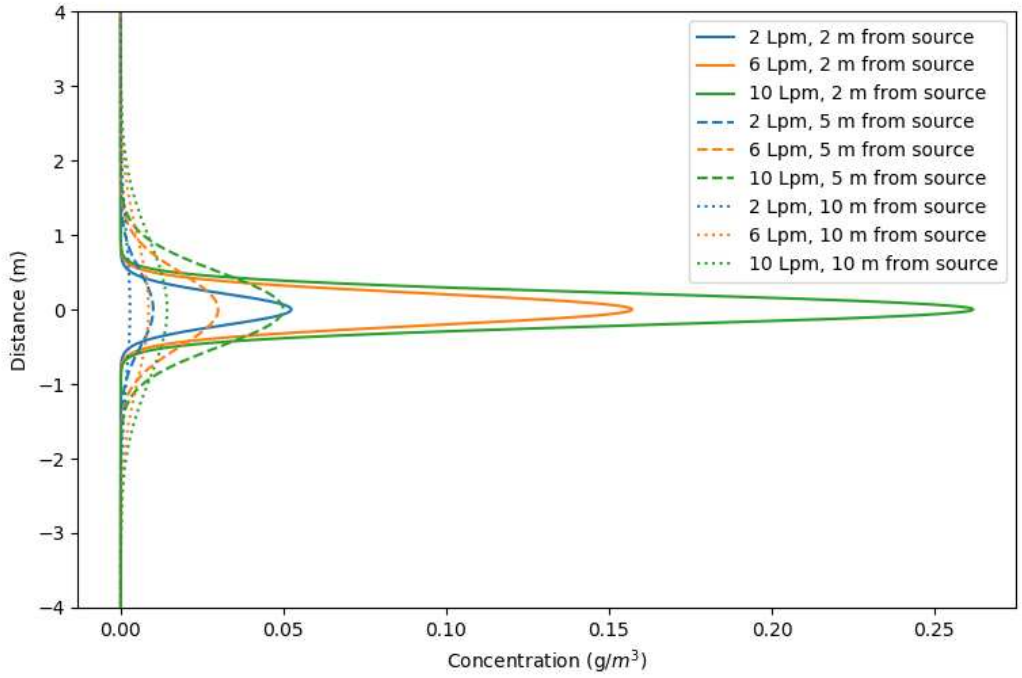

Figure 41: Concentration of CH_4 along beam path with variable with source locations and emission rates.

The release tests performed on 12/11/17 had a release rates of 2, 6 or 10 L/min at distances 2, 5 and 10 m from the beam. The releases at 10 m from the beam path are not included in this analysis. It was determined that the constant wind assumption was not valid as the fan was not strong enough to accurately transport the plume 10 m. The calculations for the comparisons are

the same as the 10/27/17 data, but the model's x-distance from the point source was changed to accommodate the release locations. Table 3 shows the comparison of the model to the experiment, with the model overestimating by a factor of 1.8. This is consistent with the expected error of a Gaussian model.

Table 3: 12/11/2017 release test, change in distance from beam and flow rate.

Distance from Beam (m)	2	5	2	5	2	5	
Flow Rate (L/min)	2	2	6	6	10	10	
Model with avg wind	0.061	0.028	0.184	0.083	0.307	0.138	
Experimental Absorbance	0.067	0.059	0.073	0.022	0.183	0.106	**Average**
Absorbance Std	*0.037*	*0.020*	*0.053*	*0.031*	*0.108*	*0.057*	0.051
Test Wind Speed (m/s)	1.247	1.159	3.247	2.900	2.026	1.844	2.070
Model/Experiment	0.911	0.466	2.505	3.709	1.674	1.307	1.762

Another comparison of the experimental (measured) absorbance and the expected (modeled) absorbance can be seen in Figure 42. The linear fit with a slope of 0.58 and an R-squared value of 75% demonstrates agreement within the dataset, but the measured absorbance values are consistently lower than the expected absorbance values. Error bars in Figure 42 represent standard deviation of absorbance for each emission. This dataset does not agree as well as the 10/27/2017 dataset which included five measured values for each expected absorbance. Some of the discrepancy in agreement can be attributed to the fewer number of tests as well as different ambient conditions.

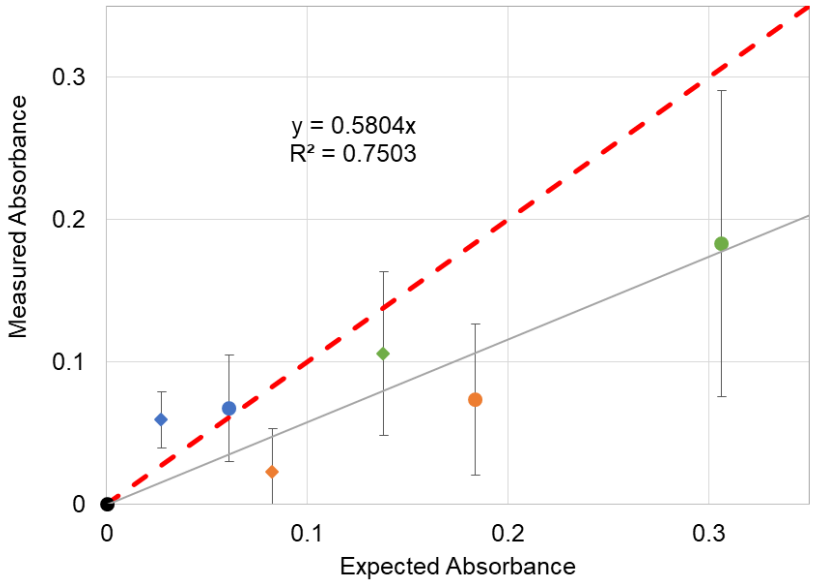

Figure 42: Measured vs expected absorbance for 12/11/2017 controlled release tests, 2 L/m (blue), 6 L/m (orange), 10 L/m green, 2 m from beam (dots), 5 m from beam (diamonds).

CHAPTER 5: Conclusions and Future Work

This chapter summarizes the conclusions from the initial field testing and development of this sensor. It evaluates how the objectives from Section 1.4 were met, and ultimately the applicability of this technology for its proposed application. The chapter will close with recommendations for continuing the development of this sensor and other suggested alternative approaches to this sensing technique.

5.1 Conclusions

The field testing was able to match a Gaussian plume model at small scales within a reasonable amount of error. Gaussian plume models can be expected to overestimate concentrations by a factor of "2-3 or even 10 fold"[51], but using a path-integrated measurement of the plume concentration averages out some of the heterogeneity that could be present in the real plume cross section[65]. Absorbance was calculated for all test configurations using the model and the measured signal from the instrument. The flow rates (2, 6, 10 L/min) correspond with the emission rates (0.02, 0.07, 0.113 g/s) used in the field testing. These rates were approximately an order of magnitude less than what was measured in the Garfield study, which was 1-100 g/s depending on the activity[22]. The variability in absorbance can be largely attributed to the varying turbulence-driven dilution ratio between the source and the beam. This variability will decrease with longer time averaging, i.e. longer emission events during testing. Given the initial test results, the significant agreement between the measurements and model provides insight into the applicability of this technology.

Emissions from the first dataset (10/27/2017) were replicated 5 times for each flow rate. The instrument had a very repeatable response to each emission despite the tests being performed

over several hours and various ambient conditions. The low average CV (~1.4%) for the baseline values reaffirms the need for an environmentally-controlled sensor environment or enclosure. Emissions at the specific test conditions for the second dataset (12/11/2017) were only measured once, but still matched the model within a reasonable amount of agreement. The standard deviation of the absorbance decreased with source distance from the beam. This is likely due to the plume having more time (and distance) to disperse in all directions, allowing for a more uniform cross section in the beam path. The Gaussian plume model is typically used for far-field measurements (~100 m up to 50 km), and with a more uniform wind field at distances greater than 5 m and longer time averaging, it is likely that our detection method would continue to have strong agreement with the model. It can be concluded that this sensor technology can be used to detect point stack sources on a small scale and the model can be used to predict future configurations.

Finally, the objectives are compared to the results from the sensor development and testing. The first objective was to "design an open-path laser absorption sensor for unspeciated hydrocarbons capable of being deployed for fence line detection at a significantly lower cost than OP-FTIR systems." The ability to detect unspeciated hydrocarbons was modeled in Chapter 2, and the field testing validated this capability with successful CH_4 detection. The option to detect non-CH_4 hydrocarbons was also successfully modeled at ICL wavelengths. The optical design resulted in a system, built only from COTS parts, capable of operating at ~100 m pathlengths. Therefore, the objective of designing to this specific application was met.

Although the cost of an initial prototype is not reflective of market costs, the developed sensor's complexity and initial costs were significantly lower than that of an OP-FTIR system, which typically cost $50,000 to $100,000 or more. With general use opto-mechanical components available in the lab (not including some support equipment), the field sensor design costs ~$2,395

(bill of materials in Table 8, Appendix). If the costs of an alignment laser, breadboard, cart, and other lab support equipment were included, the total would have been ~$21,000. By this assessment, the objective of designing a low-cost system was met and exceeded expectations.

The second objective was to "build, and test in the lab, a proof-of-concept breadboard version of the sensor," which was accomplished by the closed-cell tests in Section 3.1. Closed-cell tests validated the detection technique and aided in the development of the field sensor. The third objective was to "perform preliminary field testing to evaluate and prioritize future work that would allow the detection method to remain low-cost while advancing field capabilities." At ~1.4%, the stability of the baseline signal during ~30 min tests allows for a feasible detection of emissions similar to those modeled from the Garfield Study VOCs at 15 m (2.5-19% change in signal, Table 1). More precise detections, such as those from the 150 m case (0.6-5%, Table 2), would be challenging to detect and may require significant averaging or an improved system. The methods used for the plume model have limited accuracy of ±25%[51]. More sophisticated models could increase the understanding of potential sensor response. While the objective to perform preliminary field testing was met, several improvements could increase the sensor's capabilities. Significant lessons for improving alignment and stability were learned by fielding the sensor for the controlled release tests. The results from these tests indicated that the fielded instrument had a predictable and useful response. Consequently, future work suggestions are comprised of recommendations for improving the current design and test configurations.

5.2 Future Work

The next steps for developing this technology should focus on making improvements to three areas. The suggested improvements are intended to result in a sensor that is well-positioned

to make use of advanced plume detection. Improvements focusing on (1) more reliable alignment of the sensor, (2) optical design improvements, and (3) expanding the applications of the sensor would allow this technology to be used for advanced, continuous detection of hydrocarbon emissions from oil and gas facilities.

The baseline stabilization and field testing analysis concluded that the sensor would benefit most from reliable and consistent alignment. There are two suggested improvements that would increase reliability of the sensor's alignment. First, dedicated spaces for the sensor and the reflector with temperature control (ultimately a regulated enclosure) constitute the easiest solution for mitigating misalignment of the system. It was proven that having the sensor behind an insulated wall resulted in significant improvements in stability. Second, the inclusion of a higher power red laser (instead of the green He:Ne) represents another simple alignment improvement. This improvement would make long-path alignment feasible in daylight and facilitate operation over longer pathlengths.

There are three proposed improvements for the optical design of the sensor. First, motorized optical mounts have been used for auto-alignment in optical systems and could be used to improve the deployment of the reflector[66]. Piezoelectric actuators are commercially available on standard mounts (e.g. Thorlabs PIM1). Second, though more costly and requiring further development, an improvement would be to add reflectors in the z-direction[28]. This improvement would increase the ability to detect emissions from various heights. Third, advanced configurations and longer pathlengths are limited with the current telescope design (~100 m pathlength or less). The diameters of the current lenses limit how large the beam can be expanded. Larger collectors, like the 8" mirror used by Michel et al.[35], would be necessary for collecting larger beams—another

improvement to facilitate longer pathlengths. Other configurations using prisms and retroreflectors would be possible with a more permanent location of operation for the sensor.

There are three suggested improvements to increase the applications of the sensor. The first (and simplest) approach for improving the test setup for another application of the sensor would be to change the gas released in field tests. Tests of the current setup should be performed with a controlled release of NMVOCs in order to test this application of the sensor. According to the calculations, the current system (He:Ne laser) is capable of detecting these species at realistic concentrations. This could include a total VOC mixture or individual species. It should be noted that long term investment in this technology as a NMVOC sensor would require the replacement of the infrared He:Ne with the proposed ICL in order to minimize the interference of CH_4. Further investigation beyond the highest emitted NMVOCs (alkanes) should be performed to understand applicability to aromatics and alkenes at oil and gas facility concentrations given improvements to stability.

The second suggested improvement to expand the applications of the sensor would be to include two mid-infrared lasers or absorption lines. With the inclusion of two mid-infrared lasers or absorption lines, a differential measurement would be possible for more accurately normalizing for atmospheric turbulence, aerosols, and other interfering species[32,67]. The system could also include an in-line gas cell, with a known concentration of absorbing species, to minimize long-term drift[68]. These changes would require improvements to the DAQ system as the USB-6000 was limited by sampling rate and number of channels.

A third improvement to increase the applications of the sensor would be to have a fence line configuration of the beam path. With an improved ability to maintain alignment of the system, it would be possible to test an actual fence line configuration, i.e. have more than one reflector

enclosing the emission source. In parallel, this would require a more advanced weather station and would allow for the removal of the fan from the test setup. This would bring the test configuration much closer to the end configuration proposed for this application. Another test configuration could include measuring an area source emission similar to the EPA Ponds Study[28].

Implementing all of the above improvements would result in a sensor that could utilize machine learning to conduct advanced plume analysis. Anomalous events of interference with the open-path signal are very easy to identify with the human eye when viewing the time series data (e.g. sensor vibrations or a person walking into the beam path). Therefore, it is possible that a neural network could be trained to classify changes in signal to identify plumes[69–72]. The effort of programing a neural network for classification or plume identification has been done in many applications, but the use of machine learning requires a large and refined dataset for training. Many of the suggested test configuration improvements would be crucial for developing a consistent dataset for training a neural network capable of autonomous plume identification. This capability, when integrated with a facility's schedule for planned releases or emission events, could be a powerful tool for improving safety, saving companies money, and ultimately protecting the environment and human health.

BIBLIOGRAPHY

1. U.S. Energy Information Administration. Februray 2018 Monthly Energy Review. **0035,** 31 (2018).
2. de Gouw, J. A., Parrish, D. D., Frost, G. J. & Trainer, M. Reduced emissions of CO 2 , NOx, and SO 2 from U.S. power plants owing to switch from coal to natural gas with combined cycle technology. *Earth's Futur.* **2,** 75–82 (2014).
3. Zhang, X., Myhrvold, N. P., Hausfather, Z. & Caldeira, K. Climate benefits of natural gas as a bridge fuel and potential delay of near-zero energy systems. *Appl. Energy* **167,** 317–322 (2016).
4. Lyons, W. C. & Plisga, G. J. *Standard Handbook of Petroleum & Natural Gas Engineering*. (Gulf Professional Publishing, 2005).
5. Intergovernmental Panel on Climate Change (IPCC). *Climate Change 2014: Synthesis Report. Contribution of Working Groups I, II and III to the Fifth Assessment Report of the Intergovernmental Panel on Climate Change.* (2014). doi:10.1017/CBO9781107415324.004
6. McKenzie, L. M. *et al.* Ambient Nonmethane Hydrocarbon Levels Along Colorado's Northern Front Range: Acute and Chronic Health Risks. *Environ. Sci. Technol.* **52,** 4514–4525 (2018).
7. Volatile Organic Compounds - VOCs. *Centre Interprofessionnel Technique d'Etudes de la Pollution Atmospherique* 1–5 (2017). Available at: https://www.citepa.org/en/air-and-climate/pollutants-and-ghg/aep/vocs. (Accessed: 25th August 2017)
8. Gilman, J. B., Lerner, B. M., Kuster, W. C. & De Gouw, J. A. Source signature of volatile organic compounds from oil and natural gas operations in northeastern Colorado. *Environ.*

Sci. Technol. **47,** 1297–1305 (2013).

9. McDuffie, E. E. *et al.* Influence of oil and gas emissions on summertime ozone in the Colorado Northern Front Range. *J. Geophys. Res. Atmos.* **121,** 8712–8729 (2016).
10. Environmental Protection Agency. National Ambient Air Quality Standards for Ozone Final Rule. *Fed. Regist. (40 CFR Parts 50,51,52,53 58)* **80,** 1–7 (2015).
11. Control Techniques Guidelines for the Oil and Natural Gas Industry. *United States Environmental Protection Agency* EPA-453/B-16-001 (2016).
12. Fact Sheet: EPA's Strategy for Reducing Methane and Ozone-Forming Pollution from the Oil and Natural Gas Industry. *U.S. Environmental Protection Agency* 1–3 (2015). Available at: https://archive.epa.gov/epa/newsreleases/fact-sheet-epas-strategy-reducing-methane-and-ozone-forming-pollution-oil-and-natural.html. (Accessed: 10th December 2017)
13. McKenzie, L. M., Allshouse, W. B., Burke, T., Blair, B. D. & Adgate, J. L. Population Size, Growth, and Environmental Justice Near Oil and Gas Wells in Colorado. *Environ. Sci. Technol.* **50,** 11471–11480 (2016).
14. South Coast Air Quality Management District. *Refinery Fenceline and Community Air Monitoring*. 1–8 (http://www.aqmd.gov/home/rules-compliance/rules/scaqmd-rule-book/support-documents/rule-1180-refinery-fenceline-monitoring-plans, 2018).
15. Zavala-Araiza, D. *et al.* Super-emitters in natural gas infrastructure are caused by abnormal process conditions. *Nat. Commun.* **8,** (2017).
16. Brandt, A. R., Heath, G. A. & Cooley, D. Methane Leaks from Natural Gas Systems Follow Extreme Distributions. *Environ. Sci. Technol.* **50,** 12512–12520 (2016).
17. Marchese, A. J. *et al.* Methane Emissions from United States Natural Gas Gathering and Processing. *Environ. Sci. Technol.* **49,** 10718–10727 (2015).

18. Zimmerle, D. J. *et al.* Methane Emissions from the Natural Gas Transmission and Storage System in the United States. *Environ. Sci. Technol.* **49,** 9374–9383 (2015).

19. Environmental Protection Agency. Compendium of Methods for the Determination of Toxic Organic Compounds in Ambient Air Second Edition. *Cent. Environ. Res. Inf. Off. Res. Dev. U.S. Environ. Prot. Agency Cincinnati, OH 45268* 37 (1999). doi:EPA/625/R-96/010b

20. Environmental Protection Agency. *Method 325A—Volatile Organic Compounds from Fugitive and Area Sources: Sampler Deployment and VOC Sample Collection*. (2015). doi:10.1017/CBO9781107415324.004

21. Lamb, B., Westberg, H. & Allwine, G. Isoprene Emission Fluxes Determined by an Atmospheric Tracer Technique. *Atmos. Environ.* **20,** 1–8 (1986).

22. Collett, J. & Ham, J. *Characterizing Emissions from Natural Gas Drilling and Well Completion Operations in Garfield County , CO*. (2016).

23. Dewulf, J. & Langenhove, H. Van. Analysis of volatile organic compounds using gas chromatography. *Trends Anal. Chem.* **21,** 1–10 (2002).

24. Kessels, H., Hoogerwerf, W. & Lips, J. The Determination of Volatile Organic Compounds from EPA Method 524.2 using Purge-and-Trap Capillary Gas Chromatography, ECD, and FID. *J. Chromatogr. Sci.* **30,** 247–255 (1992).

25. Spinelle, L., Gerboles, M., Kok, G., Persijn, S. & Sauerwald, T. Review of Portable and Low-Cost Sensors for the Ambient Air Monitoring of Benzene and Other Volatile Organic Compounds. *Sensors* **17,** 1–30 (2017).

26. Collier-oxandale, A., Coffey, E., Thorson, J., Johnston, J. & Hannigan, M. Comparing Building and Neighborhood-Scale Variability of CO 2 and O 3 to Inform Deployment

Considerations for Low-Cost Sensor System Use. *Sensors* **18,** (2018).

27. Kagann, R. H., Fancher, J. D. & Tomich, S. D. Use of an Open - path FTIR Sensor to Measure VOCs at the Hanford Site. *The 87th Annual Meeting and Exhibition of the Air and Waste Management Association* (1994).

28. Thoma, E. D., Dewees, J., Modrak, M. & Hashmonay, R. *Measurement of Emissions from Produced Water Ponds : Upstream Oil and Gas Study # 1 Final Report*. *Environmental Protection Agency* (2009).

29. Sandsten, J., Weibring, P., Edner, H. & Svanberg, S. Real-time gas-correlation imaging employing thermal background radiation. *Opt. Express* **6,** 92–103 (2000).

30. Töreyin, B. U. & Çetin, A. E. Volatile Organic Compound Plume Detection Using Wavelet Analysis of Video. *5th IEEE Int. Conf. Image Process.* 1836–1839 (2008).

31. Chambers, A. K. *et al.* Direct Measurement of Fugitive Emissions of Hydrocarbons from a Refinery. *J. Air Waste Manage. Assoc.* **58,** 1047–1056 (2008).

32. Vita, F., Kern, C. & Inguaggiato, S. Development of a portable active long-path differential optical absorption spectroscopy system for volcanic gas measurements. *J. Sens. Sens. Syst.* **3,** 355–367 (2014).

33. Xia, H. *et al.* An approach of open-path gas sensor based on tunable diode laser absorption spectroscopy. *Chinese Opt. Lett.* **6,** 437–440 (2008).

34. Kosterev, A. A. & Tittel, F. K. Chemical sensors based on quantum cascade lasers. *IEEE J. Quantum Electron.* **38,** 582–591 (2002).

35. Michel, A. P. M. *et al.* Quantum cascade laser open-path system for remote sensing of trace gases in Beijing, China. *Opt. Eng.* **49,** 111125 (2010).

36. Mchale, L. E., Hecobian, A. & Yalin, A. P. Open-path cavity ring-down spectroscopy for

trace gas measurements in ambient air. *Opt. Express* **24,** 261–265 (2016).

37. Khan, M. R. R., Kang, B. H., Yeom, S. H., Kwon, D. H. & Kang, S. W. Fiber-Optic Pulse width Modulation Sensor for Low Concentration VOC Gas. *Sens. Actuators. B Chem* **188,** 689–696 (2013).

38. Thoma, E. D., Miller, M. C., Chung, K. C., Parsons, N. L. & Shine, B. C. Facility Fence-Line Monitoring Using Passive Samplers Facility Fence-Line Monitoring Using Passive Samplers. *J. Air Waste Manage. Assoc.* **61,** 834–842 (2011).

39. Chatwal, G. R. & Anand, S. K. *Spectroscopy (Atomic and Molecular)*. (Himalaya Publishing House, 2009).

40. Shirkey, R. C. & O'Brien, S. G. An Analysis of Atmospheric Aerosol Scattering for Mid-Infrared Systems. *Army Res. Lab.* **ARL-TR-393,** (2006).

41. Romanini, D., Ventrillard, I., Méjean, G., Morville, J. & Kerstel, E. Introduction to Cavity Enhanced Absorption Spectroscopy. *Springer Ser. Opt. Sci.* **179,** (2014).

42. Nowakowski, M., Wojtas, J., Blelecki, Z. & Mlkołłajczyk, J. Cavity enhanced absorption spectroscopy sensor. *Acta Phys. Pol. A* **116,** 363–367 (2009).

43. Young, C. J., Washenfelder, R. A. & Brown, S. S. Cavity Enhanced Spectroscopy: Applications, Theory and Instrumentation. *Encycl. Anal. Chem.* (2011). doi:10.1002/9780470027318.a9195

44. Stutt, C. A. *Low-Frequency Spectrum of Lock-in Amplifiers*. *Research Laboratory of Electronics, MIT* (1949).

45. Scofield, J. H. & Diagram, B. A Frequency-Domain Description of a Lock-in Amplifier. *Am. J. Phys.* **62,** 129–133 (1994).

46. Sharpe, S. W. *et al.* Gas-phase databases for quantitative infrared spectroscopy. *Appl.*

Spectrosc. **58,** 1452–1461 (2004).

47. Gordon, I. E. *et al.* The HITRAN2016 molecular spectroscopic database. *J. Quant. Spectrosc. Radiat. Transf.* **203,** 3–69 (2017).

48. Nanoplus: Nanosystems and Technologies GmbH. *Products* (2019). Available at: https://nanoplus.com/en/products/. (Accessed: 1st December 2019)

49. Canedy, C. L. *et al.* Interband cascade lasers with wavelengths spanning 2.9 μm to 5.2 μm. *J. Electron. Mater.* **37,** 1780–1785 (2008).

50. Thorlabs Inc. Helium-Neon Laser Tutorial. (2019). Available at: https://www.thorlabs.com/newgrouppage9.cfm?objectgroup_id=10776.

51. Sternberg, S. P. K. *Air Pollution: Engineering, Science and Policy*. (College Publishing, 2015).

52. Abdel-Rahman, A. A. On the atmospheric dispersion and gaussian plume model. *2nd Int. Conf. Waste Manag. Water Pollution, Air Pollution, Indoor Clim.* 31–39 (2008).

53. Stockie, J. M. The Mathematics of Atmospheric Dispersion Modeling. *SIAM Rev.* **53,** 349–372 (2011).

54. Klein, A., Witzel, O. & Ebert, V. Rapid, Time-Division multiplexed, Direct Absorption and wavelength modulation-spectroscopy. *Sensors (Switzerland)* **14,** 21497–21513 (2014).

55. Platt, U. & Stutz, J. *Differential Optical Absorption Spectroscopy, Physics of Earth and Space Environments, The Design of DOAS Instruments*. *Differential Optical Absorption Spectroscopy* **285,** (Springer-Verlag Berlin Heidelberg, 2008).

56. Fowles, G. R. *Introduction to Modern Optics*. (Dover Publications, Inc., 1975).

57. PVI-3TE Series: 2-12 μm IR Photovoltaic Detectors Thermoelectrically Cooled Optically Immersed. *Vigo Systems S.A.* (2017). Available at: https://vigo.com.pl/en/our-

products/?type=Photovoltaic. (Accessed: 10th December 2017)

58. Shemshad, J., Aminossadati, S. M. & Kizil, M. S. A review of developments in near infrared methane detection based on tunable diode laser. *Sensors Actuators, B Chem.* **171–172,** 77–92 (2012).

59. Tai, H., Tanaka, H. & Yoshino, T. Fiber-optic evanescent-wave methane-gas sensor using optical absorption for the 3.392-microm line of a He-Ne laser. *Opt. Lett.* **12,** 437–439 (1987).

60. Jacob, D., Tran, N. H., Bretenaker, F. & Lefloch, A. Differential Absorption Measurement of Methane with 2 Spatially-Resolved Laser Lines. *Appl. Opt.* **33,** 3261–3264 (1994).

61. Zurich Instruments. Principles of Lock-in Detection. 1–10 (2016). doi:10.1121/1.392931

62. Madrid, G. B. & Lopez, J. M. A. Lock-In Amplifier based on Virtual Instrumentation. *Fac. Física, Univ. Barcelona* (2016).

63. Perrin, M. Y. & Hartmann, J. M. High Temperature Absorption of the 3.39 um He-Ne Laser Line by Methane. *J. Quant. Spectrosc. Radiat. Transf.* **42,** 459–464 (1989).

64. Guiñón, J. L., Ortega, E., García-Antón, J. & Pérez-Herranz, V. Moving Average and Savitzki-Golay Smoothing Filters Using Mathcad. *Int. Conf. Eng. Educ.* (2007). doi:10.1016/j.jnoncrysol.2009.11.017

65. Herget, W. F. Validation of a method for estimating pollution emission rates from area sources using open–path ftir spectroscopy anddispersion modeling techniques. *Air Waste Manag. Assoc.* **44,** 271–279 (1994).

66. Nadler, S. D., Karecki, D. R., Mackay, G. I. & Schiff, H. I. Compact tunable diode laser spectrometer for environmental monitoring. *SPIE, Opt. Methods Atmos. Chem.* **1715,** 194–199 (1993).

67. Volkamer, R., Etzkorn, T., Geyer, A. & Platt, U. Correction of the oxygen interference with UV spectroscopic (DOAS) measurements of monocyclic aromatic hydrocarbons in the atmosphere. *Atmos. Environ.* **32,** 3731–3747 (1998).

68. Smith, C. J., Wang, W. & Wysocki, G. Real-time calibration of laser absorption spectrometer using spectral correlation performed with an in-line gas cell. *Opt. Express* **21,** 22488 (2013).

69. Mazzoni, D. *et al.* A data-mining approach to associating MISR smoke plume heights with MODIS fire measurements. *Remote Sens. Environ.* **107,** 138–148 (2007).

70. Ramirez, J. & Meyer, F. G. Machine learning for seismic signal processing: Seismic phase classification on a manifold. *Proc. - 10th Int. Conf. Mach. Learn. Appl. ICMLA 2011* **1,** 382–388 (2011).

71. Kwon, H. & Rauss, P. Feature-based ensemble learning for hyperspectral chemical plume detection. *Int. J. Remote Sens.* **32,** 6631–6652 (2011).

72. Kang, Y., Belušić, D. & Smith-Miles, K. Detecting and Classifying Events in Noisy Time Series. *J. Atmos. Sci.* **71,** 1090–1104 (2014).

APPENDIX

5.3 Controlled Release Test Summary for 10/27/2017

Table 4: 10/27/2017 controlled releases at various emission rates and 5 m from the beam.

	Flow (L/min)	Test 1	Test 2	Test 3	Test 4 (LIA)	Test 5 (LIA)	Averages
STD of baseline		0.054	0.053	0.048	0.016	0.014	0.037
MEAN baseline		3.160	3.635	3.961	1.271	1.276	2.661
CV of baseline		0.017	0.015	0.012	0.013	0.011	0.014
Modeled Absorbance (Avg Wind Speed)	2	0.031	0.031	0.031	0.031	0.031	0.031
Experimental Absorbance	2	0.055	0.052	0.033	0.038	0.029	0.042
STD of Absorbance	2	0.030	0.037	0.026	0.038	0.040	0.034
Modeled Absorbance (Avg Wind Speed)	6	0.094	0.094	0.094	0.094	0.094	0.094
Experimental Absorbance	6	0.091	0.138	0.062	0.055	0.110	0.091
STD of Absorbance	6	0.100	0.129	0.072	0.075	0.106	0.096
Modeled Absorbance (Avg Wind Speed)	10	0.156	0.156	0.156	0.156	0.156	0.156
Experimental Absorbance	10	0.089	0.115	0.127	0.189	0.248	0.154
STD of Absorbance	10	0.107	0.068	0.099	0.177	0.225	0.135
Average Wind Model / Experimental	2	0.563	0.600	0.935	0.816	1.089	0.801
	6	1.031	0.678	1.522	1.715	0.850	1.159
	10	1.750	1.353	1.231	0.825	0.630	1.158

5.4 Mixing Length Coefficients for Plume Model

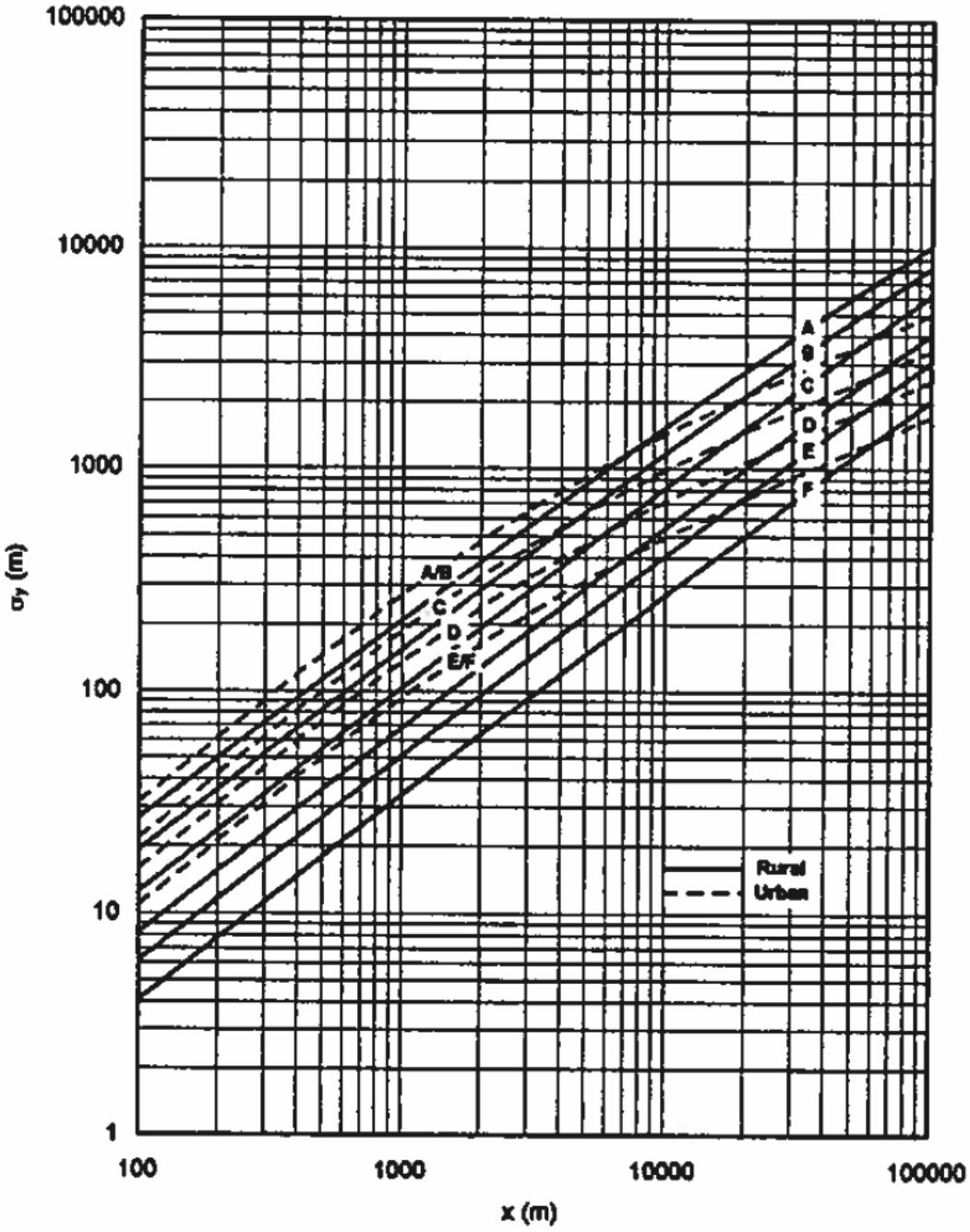

Figure 43: Rural and urban horizontal dispersion coefficients (σ_y) as a function of stability category. (Graph prepared by S.M. Claggett.)[51].

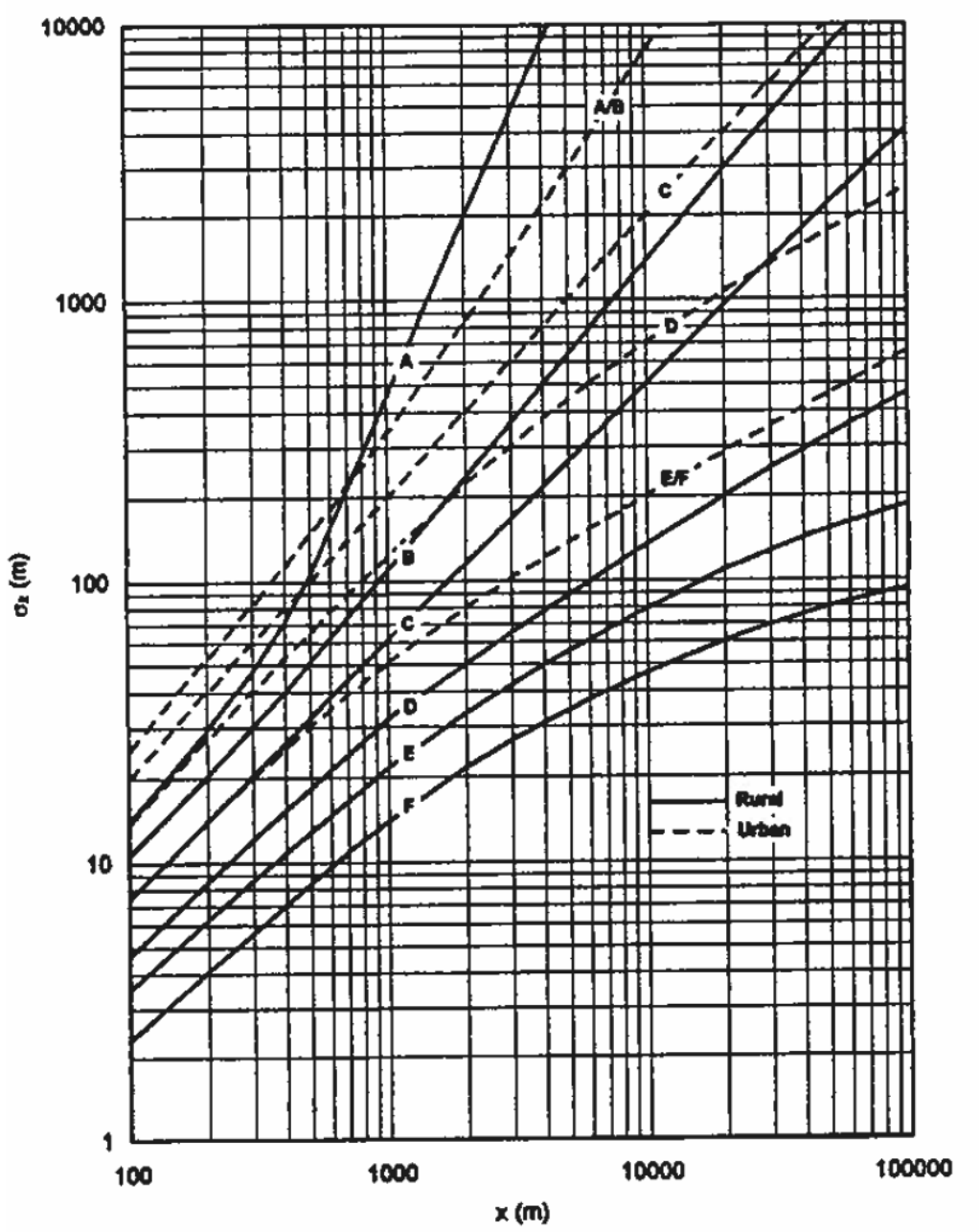

Figure 44: Rural and urban vertical dispersion coefficients (σ_z) as a function of stability category. (Graph prepared by S.M. Claggett.)[51].

Table 5: Parameters used to calculate Pasquill-Gifford σ_y[51].

Pasquill Stability Category	*c*	*d*
A	24.1670	2.5334
B	18.3330	1.8096
C	12.5000	1.0857
D	8.3330	0.72382
E	6.2500	0.54287
F	4.1667	0.36191

Table 6: Parameters used to calculate Pasquill-Gifford σ_z[51].

Pasquill Stability Category	x (km)	a	b
A*	<.10	122.800	0.94470
	0.10 – 0.15	158.080	1.05420
	0.16 – 0.20	170.220	1.09320
	0.21 – 0.25	179.520	1 12620
	0.26 – 0.30	217.410	1.26440
	0.31 – 0.40	258.890	1.40940
	0.41 – 0.50	346.750	1.72830
	0.51 – 3.11	453.850	2.11660
	>3.11	**	**
B*	<.20	90.673	0.93198
	0.21 – 0.40	98.483	0.98332
	>0.40	109.300	1.09710
C*	All	61.141	0.91465
D	<.30	34.459	0.86974
	0.31 – 1.00	32.093	0.81066
	1.01 – 3.00	32.093	0.64403
	3.01 – 10.00	33.504	0.60486
	10.01 – 30.00	36.650	0.56589
	>30.00	44.053	0.51179
E	< 10	24.260	0.83660
	.010 – 0.30	23.331	0.81956
	0.31 – 1.00	21.628	0.75660
	1.01 – 2.00	21.628	0.63077
	2.01 – 4.00	22.534	0.57154
	4.01 – 10.00	24.703	0.50527
	10.01 – 20.00	26.970	0.46713
	20.01 – 40.00	35.420	0.37615
	>40.00	47.618	0.29592
F	<.20	15.209	0.81558
	0.21 – 0.70	14.457	0.78407
	0.71 – 1.00	13.953	0.68465
	1.01 – 2.00	13.953	0.63227
	2.01 – 3.00	14.823	0.54503
	3.01 – 7.00	16.187	0.46490
	7.01 – 15.00	17.836	0.41507
	15.01 – 30.00	22.651	0.32681
	30.01 – 60.00	27.074	0.27436
	>60.00	34.219	0.21716

*If the calculated value of σ_z exceeds 5000 m, σ_z is set to 5000 m.
**σ_z is equal to 5000 m

5.5 Detector Properties

Table 7: Detector properties from Vigo Systems[57].

Parameter	PVI-2TE-5	PVI-2TE-4
Material	MCT	MCT
Type	Photovoltaic	Photovoltaic
Immersion	Immersion	Immersion
Cooling	Two-stage	Two-stage
Wavelength	5	4
Package	TO8 TO66	TO8 TO66
Window	wedged Al_2O_3	wedged Al_2O_3
Detectivity	$\geq 6,0x10^{10}$	$\geq 2,0x10^{11}$
Time constant	≤ 80	≤ 100

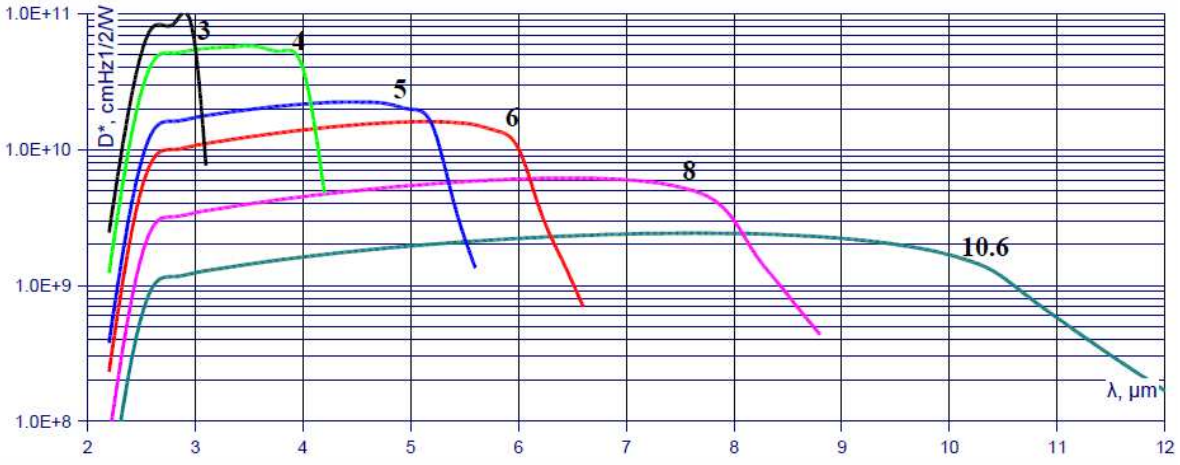

Figure 45: Detector spectral response[57].

5.6 Bill of Materials

Table 8: Bill of materials, excluding fasteners and support equipment.

PART NUMBER	DESCRIPTION	QTY.	Cost	Lab	Need	Subtotal	Cost w/o Lab parts	Link
User Library-BreadBoard	HCl Cart	1	$1,173.52	1	0	0	1173.52	https://www.thorlabs.com/thorproduct.cfm?partnumber=B2436F
8020 Cart	Mobile Cart	1	$300.00	1	0	0	300	Estimation from 8020 Examples
Casters	Casters and HW	1	$336.73	0	1	336.73	336.73	https://8020.net/2714.html
HeNe 3um	HeNe 3um	1	3614	1	0	0	3614	Newport Dual HeNe IR
CP360R	Beam Split mount	1	93.8	0	1	93.8	93.8	https://www.thorlabs.com/thorproduct.cfm?partnumber=CP360R
LCP02-Step	1"-2" adapter	2	39	0	2	78	78	https://www.thorlabs.com/thorproduct.cfm?partnumber=LCP02
50mmLensEdmundConvexPlano	150FI 2" CaF2 lens	2	395	0	2	790	790	http://www.edmundoptics.com/optics/optical-lenses/plano-convex-pcx-spherical-singlet-lenses/calcium-fluoride-plano-convex-pcx-lenses/88169/
LCPMA2	Snap bracket 60mm	4	35.8	0	4	143.2	143.2	https://www.thorlabs.com/thorproduct.cfm?partnumber=LCPMA2
LCP01B	slide 60mm bracket	4	29.8	0	4	119.2	119.2	https://www.thorlabs.com/thorproduct.cfm?partnumber=LCP01B
1inMirror	steer mirror	6	51	6	0	0	306	https://www.thorlabs.com/thorproduct.cfm?partnumber=PF10-03-G01
FM90-Step	flip mirror mount	1	82	1	0	0	82	https://www.thorlabs.com/thorproduct.cfm?partnumber=FM90
KM100	1" mirror mounts	6	38.7	6	0	0	232.2	https://www.thorlabs.com/newgroupage9.cfm?objectgroup_id=1492&pn=KM100#789
MPD129-M01-Solidworks	off axis parabolic mirror	1	194	1	0	0	194	https://www.thorlabs.com/thorproduct.cfm?partnumber=MPD129-M01
Detector	detectors	2	5000	2	0	0	10000	https://vigo.com.pl/en/our-products/?optimal_wavelength=%3C8
HeNeGreen	alignment laser	1	1952	1	0	0	1952	https://www.newport.com/f/green-hene-lasers-543-nm
RS1.5P	1" mount L=1.5	8	24.3	5	3	72.9	194.4	https://www.thorlabs.com/thorproduct.cfm?partnumber=RS1.5P
VC3C	v mounts for hene	4	38	2	2	76	152	https://www.thorlabs.com/thorproduct.cfm?partnumber=VC3C#ad-image-0
RS2M	spacers for under hene (vmounts)	4	6.7	0	4	26.8	26.8	https://www.thorlabs.com/thorproduct.cfm?partnumber=RS2M
SPT2	2" MIRROR MNT	2	65	0	2	130	130	https://www.thorlabs.com/thorproduct.cfm?partnumber=SPT2
SM1Z	z trans stage	2	190	2	0	0	380	https://www.thorlabs.com/thorproduct.cfm?partnumber=SM1Z
AD1	1/2" optic adapter	2	15.3	0	2	30.6	30.6	https://www.thorlabs.com/thorproduct.cfm?partnumber=AD1
CP06	30mm cage to 1" optic (mounts	2	17.1	2	0	0	34.2	https://www.thorlabs.com/newgroupage9.cfm?objectgroup_id=2273&pn=CP06#2869
BA1S	bases	9	5.2	9	0	0	46.8	https://www.thorlabs.com/thorproduct.cfm?partnumber=BA1S
TR1	1/2" post L=1	7	4.74	0	7	33.18	33.18	https://www.thorlabs.com/thorproduct.cfm?partnumber=TR1
TR30_M	metric for det (1/2"post) L=30mm	2	4.74	0	2	9.48	9.48	https://www.thorlabs.com/thorproduct.cfm?partnumber=TR30/M
PH1.5	1/2"post holder L=1.5	9	7.22	0	9	64.98	64.98	https://www.thorlabs.com/thorproduct.cfm?partnumber=PH1.5#ad-image-0

TRP1-Step	pedistal mounts for flip mirror	1	18.8	0	1	18.8	18.8	https://www.thorlabs.com/thorproduct.cfm?partnumber=TRP1
MSC2-Step	ped mount holder for flip mirror	1	15.3	0	1	15.3	15.3	https://www.thorlabs.com/thorproduct.cfm?partnumber=MSC2
ER6 4 pack	6" rod	1	32.2	1	0	0	32.2	https://www.thorlabs.com/thorproduct.cfm?partnumber=ER6-P4
ER10	10" rod	8	12.7	0	8	101.6	101.6	https://www.thorlabs.com/thorproduct.cfm?partnumber=ER10
ER8 4 pacl	8" rod	1	44.46	0	1	44.46	44.46	https://www.thorlabs.com/thorproduct.cfm?partnumber=ER8-P4
LA5315	1/2" caf2 lens, 20mm fl	2	105	0	2	210	210	https://www.thorlabs.com/thorproduct.cfm?partnumber=LA5315
					Totals	**2395.03**	**20939.45**	